

SIMULATING GRAIN SHAPE EFFECTS AND DAMAGE IN GRANULAR MEDIA USING PERIDEM *

DEBDEEP BHATTACHARYA[†] AND ROBERT P. LIPTON[‡]

Abstract. We provide a numerical platform for the analysis of particle shape and topology effect on the macroscopic behavior of granular media. We work within a Discrete Element Method (DEM) framework and apply a peridynamic model for deformable particles accounting for deformation and damage of individual particles. To accommodate arbitrary particle shapes including nonconvex ones as well as particle topology, an efficient method is developed to keep intra-particle peridynamic interaction within particle boundaries. Particle contact with the rigid boundary wall is computed analytically to improve accuracy. To speed up simulations with particles of different shapes and sizes the initial configuration is chosen using security disks containing different particle shapes that are placed in a jammed state using an optimization-based method. The effect of particle shape and topology on settling and compaction of the aggregate for deformable particles is analyzed.

Key words. peridynamics, damage, granular media, grain shape, DEM

AMS subject classifications. 70-08, 70-10, 74A70, 74R10

1. Introduction. Granular media simulations are important for many industrial and geophysical applications. The discrete element method (DEM) introduced by Cundall and Strack [7], provides one framework for granular simulation assuming that particle shapes are rigid. DEM is a molecular dynamics (MD) model for particles on a representative volume and is used to capture macroscopic transport properties [29] of particle aggregates. The method discussed here is a direct generalization of the DEM method introduced by Cundall and Strack [7] for modeling granular assemblies. The scope of the DEM method addresses applications ranging from rock crushing [17] and powder rheology [8], to the modeling of vehicles traveling over gravel pavements [33]. Here each rigid particle in the aggregate satisfies Newton’s second law of motion applied to particle centers and interacts with other particles through contact forces.

While DEM-based approaches capture the rigid motion of the particle boundaries they do not account for the deformation of individual grains. In addition DEM does not capture complex damage propagation based on each particle’s geometry, nor the effects of notched or pre-cracked particles. Hence capturing the elastic and inelastic deformation of individual grains will lead to improved models for granular media. With this in mind the “peridynamic” models introduced by Silling [37] are a nonlocal reformulation of continuum mechanics that model elastic deformation but also model fracture growth as an emergent behavior. Recently, peridyamic models have been used for mesoscale modeling of granular media, especially for capturing elastic and inelastic deformation and intra-granular force within individual grains. Behzadinasab et. al. [2] studied shockwave perturbation decay in particle beds of circular grains. Zhu and Zhao [42, 43] used a Weibull statistics-peridynamics approach to investigate crushing piles of sand. In recent joint work the authors combined the direct element method (DEM) with peridynamics (PeriDEM) to the study of granular flows see, Jha

*

Funding: This material is based upon work supported by the U. S. Army Research Laboratory and the U. S. Army Research Office under Contract/Grant Number W911NF-19-1-0245.

[†] Department of Mathematics, Louisiana State University, Baton Rouge, Louisiana 70803 (deb-deepbh@lsu.edu).

[‡] Department of Mathematics, LSU Center of Computation & Technology, Louisiana State University, Baton Rouge, Louisiana, 70803 (lipton@lsu.edu)

et. al. [20].

The effects of particle shapes on large aggregates have been of recent interest. In [1, 31] authors performed triaxial compression tests on 3D printed shapes to study the stress response of granular packing of various shapes. Hafez et al [15] also experimentally studied the effect of particle shapes in particle discharge or clogging. Using LS-DEM simulations [24] captured the shear banding of sand by modeling the shapes of individual sand grains. Motivated by these considerations we enhance and flesh out the PeriDEM method as a computational platform to assess the effect of particle shape and topology on the aggregate motion of particle beds as influenced by intra-granular elastic deformation and damage. This provides the opportunity to investigate the motion of the aggregate as a function of the physical properties of the particles and their geometry.

In the context of this paper, particles are no longer rigid and all points inside each particle interact with each other peridynamically. This allows for both elastic and inelastic particle deformation. As in DEM the particles interact with other particles through frictional contact forces but now rephrased for deformable particles in an appropriate way. We systematically address all contact forces, friction, and damping to account for interaction between deformable particles in Subsection 4.1 through Subsection 4.3. The transition between static and dynamic friction, i.e. sliding-sticking friction is captured in Subsection 4.2. Force interaction between newly formed components of a shattered particle are given in Subsection 4.4. The force interaction between particles and container walls is given in Subsection 4.5. Our treatment of peridynamic forces for non convex particles is given in Section 5. We note that in order to compare the macroscopic effects associated with assemblages of particles of different shape, it is essential to start the dynamics from an initial particle configuration that is agnostic to particle shape. To realize such a initial configuration we require the maximum cross-sectional diameter of every particle to be a fixed constant across all shapes. Additionally the location of the center point of this diameter is prescribed so each particle experiences no interaction force from any other particle or the container walls. Lastly the particles are randomly oriented. To accomplish this we employ the notion of non overlapping security spheres containing one particle each. The methodology behind this construction is given in Subsection 7.1. In summary the combination of intra-particle and inter-particle interaction allows for particle comminution and crushing as part of the dynamic rheology. As an example one can think of dense but loosely packed particle aggregates as seen in pebble or sandy roadbeds subject to vehicular traffic.

As with MD and DEM our simulations illustrate how macroscopic properties can be obtained from microscopically dynamic simulations. We begin by discussing time integration and the choice of time step to insure stability in simulations in Subsection 6.1. It is pointed out here that the current numerical simulations focus on two dimensional problems. A series of numerical experiments on particle beds/aggregates involving different particle shapes are carried out. The goal is to provide a new opportunity to examine effect of shape and topology on macroscopic properties from microstructural dynamics. Here we illustrate how the use of particles with convex shapes such as spheres and squares differ from non convex shapes such as crosses and more generally rough shapes with re-entrant corners. We start computing the solution to initial value problems for two and three particles in Section Section 6. Here we execute two particle collisions with fracture corresponding to the Kalthoff Winkler experiment. In this experiment a rectangular particle *the impactor* collides head on with a stationary notched (hence non-convex) particle, see Subsection 6.2. The exper-

imentally observed fracture pattern is recovered by our numerical simulation of two particles using the peridynamic intra-particle model and the nonlocal contact model. This provides a corroboration between experiment and the intra-particle deformation and particle to particle contact model for convex and non-convex particles. Next we illustrate the effect of horizon size on the damage zone for particle fracture for colliding cross shaped particles in [Subsection 6.3](#). The generation of non-interpenetrating child particles and non-interpenetration of fissures under compression fracture is illustrated over a range of fracture toughness's in [Subsection 6.4](#).

As examples involving particle aggregates we provide numerical simulations showing the relative effect of particle geometry and topology on macroscopic quantities. The dynamic settling simulations of [\[27, 34\]](#) using DEM are carried out and are found to produce realistic structural information as obtained through experiment [\[11\]](#). Motivated by this we perform numerical simulations for the settling of particle columns made from deformable particles with different shapes and topology under gravitational forces. The reaction force on the wall of the particle containers is computed and the effect of particle shape is illustrated, see [Subsection 7.3](#). Next we apply our approach to particles of variable shape and topology exhibiting both inelastic and elastic behavior inside each grain. This allows us to incorporate effects of grain shape and topology through both particle deformation and particle damage. We simulate aggregates subject to dynamic compaction undergoing deformation and damage that highlight these features are provided in [Subsection 7.4](#). The new methods introduced here provide the tools to study and to design particle shape and topology for desired macroscopic effects not just in the elastic regime, but also when individual grains suffer damage.

2. Overview of capturing intra-particle deformation and inter-particle interaction and particle interaction with container. We introduce a particle model of hybrid type for modeling particle aggregates. This method was initiated by the authors together with coauthors in the joint work [\[20\]](#). The method includes elastic and inelastic effects inside each particle as well as inter particle interaction and boundary effects. This paper extends the methodology and provides new modeling capability for particle crushing and domains containing the aggregate that change shape with time, as well as eliminating numerical instabilities inherent in sliding friction. Let $\Omega \in \mathbb{R}^d$ denote the domain containing the particle assemblage where $d = 2$ or 3 is the dimension. The assemblage consists of N particles $D_i \subset \Omega$, $i = 1, 2, \dots, N$. The time-evolution of particle D_i in the media is given by $D_i(t)$, $t \in [0, T]$ with $D_i(0) = D_i$. Let $\mathbf{x} \in D_i(0)$ denote the coordinates of a material point in the particle in the reference configuration which is taken to be the initial configuration and let $\mathbf{u} : D_i(0) \times [0, T] \rightarrow \mathbb{R}^d$ and $\mathbf{v} : D_i(0) \times [0, T] \rightarrow \mathbb{R}^d$ denote the displacement and velocity fields. At any time $t \in [0, T]$ the coordinates of the material point $\mathbf{p} = \mathbf{p}(\mathbf{x}, t)$ inside $D_i(t)$ is given by $\mathbf{p}(\mathbf{x}, t) = \mathbf{x} + \mathbf{u}(\mathbf{x}, t)$ and $\mathbf{v}(\mathbf{x}, t) = \dot{\mathbf{u}}(\mathbf{x}, t)$. The particles are subjected to external forces such as gravitational acceleration and moving container walls that dynamically alter the position of particles. There are two different interactions in the particle media: intra-particle interaction in which each particle reacts to forces on its boundary, these drive the evolution of internal forces inside each particle; and the inter-particle interaction in which particles come into contact and exchange forces at their interface as well as boundary forces imparted on the particles by moving rigid domain walls. For the former we consider the peridynamic description of solid deformation. For the latter, we propose a Peridynamics-DEM like model to account for exchange of force between particles and domain walls. Since

contact in the model is defined at the level of material points in the neighborhood of the contact region, the model can be used to describe contact for arbitrarily shaped particles and particles of different topology.

The dynamics of the particle assemblage is given by an interacting particle system and in this way described by the dynamics of each particle. The motion of a particle aggregate inside Ω is given by Newton's second law of motion:

$$(2.1) \quad \rho \ddot{\mathbf{u}}(\mathbf{x}, t) = \mathbf{F}_i^{int}(\mathbf{x}, t; \mathbf{u}) + \mathbf{F}_i^{ext}(\mathbf{x}, t; \mathbf{u}), \quad \forall (\mathbf{x}, t) \in D_i \times [0, T], \text{ for } i = 1, \dots, N.$$

where ρ is the mass density of the particle, $\mathbf{F}_i^{int}(\mathbf{x}, t, \mathbf{u}(\mathbf{x}, t))$ are the forces inside $D_i(t)$ and $\mathbf{F}_i^{ext}(\mathbf{x}, t)$ are the external forces on the i^{th} particle such as inter-particle contact force or a moving container wall acting on the particles. We close the above system by specifying an initial condition on the displacement $\mathbf{u}(\mathbf{x}, 0) = \mathbf{u}_0(\mathbf{x})$ and velocity $\dot{\mathbf{u}}(\mathbf{x}, 0) = \mathbf{v}_0(\mathbf{x})$ for all $\mathbf{x} \in D_i$, $i = 1, \dots, N$. In this way we have framed the particle dynamics for the assemblage as an initial value problem for a displacement field $\mathbf{u}(\mathbf{x}, t)$ for $\mathbf{x} \in D_i$, $i = 1, \dots, N$ and $t \in [0, T]$ where the details of the intra and inter-particle forces acting on $D_i(t)$ depend on $\mathbf{F}_i^{int}(\mathbf{x}, t; \mathbf{u})$ and $\mathbf{F}_i^{ext}(\mathbf{x}, t; \mathbf{u})$. In the next sections we show the specific form of \mathbf{F}_i^{int} and \mathbf{F}_i^{ext} used for capturing intra-particle deformation and inter-particle interaction and interaction with container.

3. Peridynamic intra-particle force model. To model both elastic and inelastic effects inside a particle viewed as a continuum we opt for a nonlocal modelling approach. The forces acting on a point $\mathbf{p}(\mathbf{x}, t)$ inside the i^{th} particle domain $D_i(t) \subset \mathbb{R}^2$ is given by the integro-differential equation

$$(3.1) \quad \mathbf{F}_i^{int}(\mathbf{x}, t; \mathbf{u}) = \int_{H_\epsilon(\mathbf{x}) \cap D_i} \mathbf{f}(\mathbf{u}(\mathbf{x}', t), \mathbf{u}(\mathbf{x}, t), \mathbf{x}', \mathbf{x}, t) dV_{\mathbf{x}'},$$

where \mathbf{f} is the force density function between pairs of points. The peridynamic *horizon* is defined as the set $H_\epsilon(\mathbf{x}) = \{\mathbf{x}' \in \mathbb{R}^2 : |\mathbf{x}' - \mathbf{x}| \leq \epsilon\}$. For a material point $\mathbf{x}' \in H_\epsilon(\mathbf{x}) \cap D_i$, $V_{\mathbf{x}'}$ denotes the volume element associated with \mathbf{x}' . Here the force density has the units force per unit volume² or *area*² depending on the dimension and the first term on the right hand side of Equation (3.1) is the total force exerted on \mathbf{x} by its surrounding neighborhood. Here the force density is given for two-point interactions. This is called bond-based peridynamics [37]. Given $\mathbf{x} \in D_i$ and $\mathbf{x}' \in H_\epsilon(\mathbf{x}) \cap D_i$, the vector $\boldsymbol{\xi} = \mathbf{x}' - \mathbf{x}$ is referred to as a *bond*. Defining $\boldsymbol{\eta} = \mathbf{u}(\mathbf{x}', t) - \mathbf{u}(\mathbf{x}, t)$, the *stretch* s associated with a bond $\boldsymbol{\xi}$ is defined as $s = s(\mathbf{u}(\mathbf{x}', t), \mathbf{u}(\mathbf{x}, t), \mathbf{x}', \mathbf{x}) := \frac{|\boldsymbol{\xi} + \boldsymbol{\eta}| - |\boldsymbol{\xi}|}{|\boldsymbol{\xi}|} = \frac{|\mathbf{p}(\mathbf{x}', t) - \mathbf{p}(\mathbf{x}, t)| - |\mathbf{x}' - \mathbf{x}|}{|\mathbf{x}' - \mathbf{x}|}$.

Next we describe the constitutive law relating force density to stretch between two points. A microelastic material considered in [3] is given by the pairwise force density function \mathbf{f} of the form

$$(3.2) \quad \mathbf{f} = \begin{cases} c_w w(|\boldsymbol{\xi}|) s \frac{\boldsymbol{\xi} + \boldsymbol{\eta}}{|\boldsymbol{\xi} + \boldsymbol{\eta}|} & \text{if } |\boldsymbol{\xi}| < \epsilon \\ 0 & \text{otherwise,} \end{cases}$$

where the *micromodulus function* $w(r)$ is a non-negative scalar function that is non-increasing in r . The peridynamic spring constant c_w is chosen such that the integral operator agrees with the Cauchy-Navier operator up to the second order. We list the value of the peridynamic spring constant and two micromodulus functions in Table 1. The model with constant micromodulus is called the Prototype Microelastic Brittle (PMB) material and was introduced in [36].

3.1. Irreversible damage and memory. The bond ξ between \mathbf{x} and \mathbf{x}' is broken at time t if the stretch $s(\mathbf{u}(\mathbf{x}', t), \mathbf{u}(\mathbf{x}, t), \mathbf{x}', \mathbf{x})$ exceeds the *critical stretch* s_0 in the absolute value, i.e. when $|s| > |s_0|$. The value of s_0 is determined by equating the critical energy release rate G_c with the total energy required to sever all bonds across a crack surface of unit area. In [Table 1](#), we list the value of the critical stretch for both “constant” and “conic” micromodulus functions [\[14\]](#). Once a bond is broken at time $t = t_0$, it remains broken for all time $t > t_0$. The *damage* of a material point \mathbf{x} is defined as the ratio of the number of broken bonds connected to \mathbf{x} at time t to the number of bonds connected to \mathbf{x} in the reference configuration (i.e. at $t = 0$).

Table 1: Peridynamic spring constant for various choices the micromodulus function in [Equation \(3.2\)](#).

Type	$w(\xi)$	c_w	$c_w w(\xi)$	s_0
Constant	1	$\frac{6E}{\pi\epsilon^3(1-\nu)}$	$\frac{6E}{\pi\epsilon^3(1-\nu)}$	$\sqrt{\frac{4\pi G_c}{9E\epsilon}}$
Conic	$\left(1 - \frac{ \xi }{\epsilon}\right)$	$\frac{24E}{\pi\epsilon^3(1-\nu)}$	$\frac{24E}{\pi\epsilon^4(1-\nu)} (\epsilon - \xi)$	$\sqrt{\frac{5\pi G_c}{9E\epsilon}}$

REMARK 1. *Because bond-based peridynamics is a two-point interaction model the Poisson ratio is $\frac{1}{3}$ in 2D and $\frac{1}{4}$ in 3D [\[40\]](#). While this limitation can be easily overcome by using a state-based model [\[39\]](#), we do not pursue that here.*

In the following section we introduce the different inter particle forces and wall forces then combine them with [Equation \(3.1\)](#) to get the equation of evolution for every particle in the aggregate given in [Subsection 4.6](#).

4. Contact model. To capture the inter grain interactions we apply the short-range contact force model used by [\[36\]](#) and [\[2\]](#). In the short-range contact model, two material points belonging to two different peridynamic bodies are said to be in contact if they are within a certain distance R_c , called the *contact radius*. Let D_i and D_j be two particles ($i \neq j$) and $\mathbf{p}(\mathbf{x}, t) \in D_i(t)$ and $\mathbf{p}(\mathbf{y}, t) \in D_j(t)$. We define the *normal direction* $\mathbf{e}(\mathbf{y}, \mathbf{x}, t)$ by the unit vector $\mathbf{e}(\mathbf{y}, \mathbf{x}, t) = \frac{\mathbf{p}(\mathbf{y}, t) - \mathbf{p}(\mathbf{x}, t)}{|\mathbf{p}(\mathbf{y}, t) - \mathbf{p}(\mathbf{x}, t)|}$ which denotes the direction from \mathbf{x} to \mathbf{y} .

4.1. Repulsive contact force. The short-range repulsive force $\mathbf{F}_r(\mathbf{y}, \mathbf{x}, t)$ exerted on $\mathbf{p}(\mathbf{x}, t) \in D_i(t)$ by $\mathbf{p}(\mathbf{y}, t) \in D_j(t)$ (see [\[36, 2, 20\]](#)) is given by

$$(4.1) \quad \mathbf{F}_r(\mathbf{y}, \mathbf{x}, t) = \begin{cases} -K_n(R_c - |\mathbf{p}(\mathbf{y}, t) - \mathbf{p}(\mathbf{x}, t)|)V_{\mathbf{x}}V_{\mathbf{y}}\mathbf{e}(\mathbf{y}, \mathbf{x}, t) & \text{if } |\mathbf{p}(\mathbf{y}, t) - \mathbf{p}(\mathbf{x}, t)| < R_c \\ 0 & \text{otherwise} \end{cases}$$

where the normal contact stiffness is $K_n = \frac{18k}{\pi\epsilon^5}$, where k is the bulk modulus, $V_{\mathbf{x}}$ and $V_{\mathbf{y}}$ are volume elements associated with \mathbf{x} and \mathbf{y} , respectively [\[2, 20\]](#). When the participating peridynamic bodies have bulk moduli k_1 and k_2 , respectively, an effective bulk modulus is used and given by the harmonic mean, i.e. $k = \frac{2k_1k_2}{k_1+k_2}$ [\[20\]](#). Here the repulsive force is chosen to be linear in the distance between the points in contact. A nonlinear relation is also possible but over short distances they are comparable [\[8\]](#).

We conclude from [Equation \(4.1\)](#) that the total repulsive force on a point $\mathbf{p}(\mathbf{x}, t) \in$

$D_i(t)$ due to all neighboring particles is given by

$$(4.2) \quad \sum_{j \neq i} \int_{\{\mathbf{y} \in D_j : |\mathbf{p}(\mathbf{y}, t) - \mathbf{p}(\mathbf{x}, t)| < R_c\}} \mathbf{f}_r(\mathbf{y}, \mathbf{x}, t) dV_{\mathbf{y}}, \quad \text{where } \mathbf{f}_r = \frac{\mathbf{F}_r}{V_{\mathbf{x}}}.$$

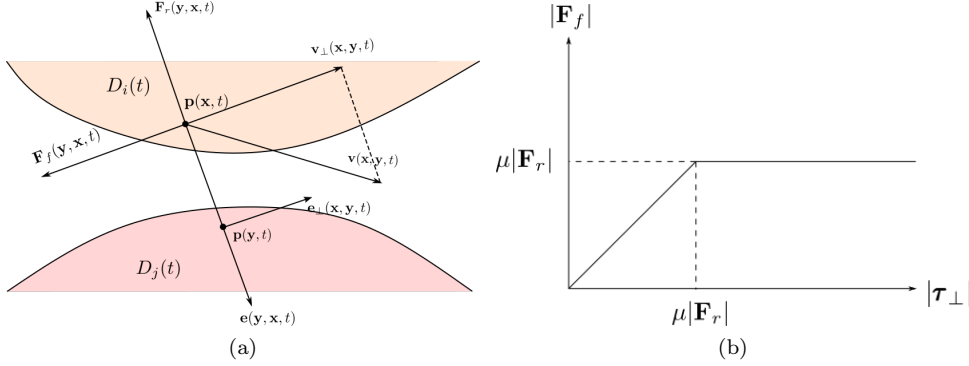


Fig. 1: (a) Geometric picture for friction force (b) Friction force vs the prescribed tangential force and the transition between sticking and slipping regimes.

4.2. Nonlocal friction. A tangential damping force is incorporated for nodes in contact to model energy dissipation due to friction using Coulomb's law. Such forces are incorporated in DEM models in terms of virtual spring displacement (see, for example, [29]). To capture the stick/slip transition in our dynamic friction model, we follow the approach of regularized Coulomb's model [30, 6] adapted to the nonlocal setting. Let the relative velocity of $\mathbf{p}(\mathbf{x}, t) \in D_i(t)$ with respect to $\mathbf{p}(\mathbf{y}, t) \in D_j(t)$ be $\mathbf{v}(\mathbf{x}, \mathbf{y}, t) = \dot{\mathbf{u}}(\mathbf{x}, t) - \dot{\mathbf{u}}(\mathbf{y}, t)$. The tangential component of the relative velocity of $\mathbf{p}(\mathbf{x}, t)$ with respect to $\mathbf{p}(\mathbf{y}, t)$ is therefore given by $\mathbf{v}_{\perp}(\mathbf{x}, \mathbf{y}, t) = \mathbf{v}(\mathbf{x}, \mathbf{y}, t) - (\mathbf{v}(\mathbf{x}, \mathbf{y}, t) \cdot \mathbf{e}(\mathbf{y}, \mathbf{x}, t)) \mathbf{e}(\mathbf{y}, \mathbf{x}, t)$. We define the tangential contact direction by $\mathbf{e}_{\perp}(\mathbf{x}, \mathbf{y}, t) = \frac{\mathbf{v}_{\perp}(\mathbf{x}, \mathbf{y}, t)}{|\mathbf{v}_{\perp}(\mathbf{x}, \mathbf{y}, t)|}$, see Figure 1a. The friction force $\mathbf{F}_f(\mathbf{y}, \mathbf{x}, t)$ on $\mathbf{p}(\mathbf{x}, t)$ due to $\mathbf{p}(\mathbf{y}, t)$ depends on the prescribed tangential force $\boldsymbol{\tau}_{\perp}(\mathbf{x}, \mathbf{y}, t)$ on $\mathbf{p}(\mathbf{x}, t)$ in the direction $\mathbf{e}_{\perp}(\mathbf{x}, \mathbf{y}, t)$. In the sticking regime i.e., when $|\boldsymbol{\tau}_{\perp}(\mathbf{x}, \mathbf{y}, t)| \leq \mu |\mathbf{F}_r(\mathbf{y}, \mathbf{x}, t)|$, the friction force acts as a restoring force to prevent the motion of $\mathbf{p}(\mathbf{x}, t)$ with respect to $\mathbf{p}(\mathbf{y}, t)$. In the slipping regime, i.e., when $|\boldsymbol{\tau}_{\perp}(\mathbf{x}, \mathbf{y}, t)| > \mu |\mathbf{F}_r(\mathbf{y}, \mathbf{x}, t)|$, the friction force has a constant magnitude of $\mu |\mathbf{F}_r(\mathbf{y}, \mathbf{x}, t)|$ and acts in the opposite direction of $\mathbf{v}_{\perp}(\mathbf{x}, \mathbf{y}, t)$. The transition of the friction force between the sticking and slipping regime depending on the prescribed tangential force is shown in Figure 1b. As in [30], the stick/slip transition in our model is characterized by the relative speed $|\mathbf{v}_{\perp}(\mathbf{x}, \mathbf{y}, t)|$ crossing a speed threshold v_{thr} . Here, v_{thr} is taken to be depending on the numerical time step Δt and is given by $v_{\text{thr}}(\mathbf{x}, \mathbf{y}, t, \Delta t) = \frac{\mu}{\rho V_{\mathbf{x}}} |\mathbf{F}_r(\mathbf{y}, \mathbf{x}, t)| \Delta t$, which is obtained by approximating the maximal magnitude of $\mathbf{v}_{\perp}(\mathbf{x}, \mathbf{y}, t)$ resulting from the prescribed tangential force $\boldsymbol{\tau}_{\perp}(\mathbf{x}, \mathbf{y}, t) = \mu |\mathbf{F}_r(\mathbf{y}, \mathbf{x}, t)| \mathbf{e}_{\perp}(\mathbf{x}, \mathbf{y}, t)$ in the absence of friction. Note that $v_{\text{thr}}(\mathbf{x}, \mathbf{y}, t, \Delta t) \rightarrow 0$ as $\Delta t \rightarrow 0$.

The frictional force \mathbf{F}_f on $\mathbf{p}(\mathbf{x}, t) \in D_i(t)$ due to $\mathbf{p}(\mathbf{y}, t) \in D_j(t)$ is given by

$$(4.3) \quad \mathbf{F}_f(\mathbf{y}, \mathbf{x}, t) = \begin{cases} -\mu |\mathbf{F}_r(\mathbf{y}, \mathbf{x}, t)| \mathbf{e}_\perp(\mathbf{y}, \mathbf{x}, t), & \text{if } |\mathbf{v}_\perp(\mathbf{x}, \mathbf{y}, t)| > v_{\text{thr}}(\mathbf{x}, \mathbf{y}, t, \Delta t) \\ -\frac{1}{\epsilon_f} |\mathbf{v}_\perp(\mathbf{x}, \mathbf{y}, t)| \mathbf{e}_\perp(\mathbf{y}, \mathbf{x}, t), & \text{if } 0 \leq |\mathbf{v}_\perp(\mathbf{x}, \mathbf{y}, t)| \leq v_{\text{thr}}(\mathbf{x}, \mathbf{y}, t, \Delta t), \end{cases}$$

where ϵ_f is a Δt -dependent regularization parameter given by $\epsilon_f = \frac{\Delta t}{\rho V_{\mathbf{x}}}$. ϵ_f is chosen so that once $|\boldsymbol{\tau}_\perp(\mathbf{x}, \mathbf{y}, t)| \leq \mu |\mathbf{F}_r(\mathbf{y}, \mathbf{x}, t)|$, the relative velocity of $\mathbf{p}(\mathbf{x}, t)$ reduces to zero in the next iteration. Related regularized nonlocal tangential dynamic friction models that employ [30] between particles are introduced in [23].

Consequently, the total friction force on the point $\mathbf{p}(\mathbf{x}, t) \in D_i(t)$ due to all the neighboring particles is given by

$$(4.4) \quad \sum_{j \neq i} \int_{\{\mathbf{y} \in D_j: |\mathbf{p}(\mathbf{y}, t) - \mathbf{p}(\mathbf{x}, t)| < R_c\}} \mathbf{f}_f(\mathbf{y}, \mathbf{x}, t) dV_{\mathbf{y}}, \quad \text{where } \mathbf{f}_f = \frac{\mathbf{F}_f}{V_{\mathbf{x}}}.$$

Note that the frictional force is dependent on relative velocity between points taken from different particles in contact and is implemented using the velocity-Verlet scheme described in [Subsection 6.1](#).

4.3. Normal damping force. In this implementation we incorporate normal damping to allow energy dissipation upon normal contact between particles. The damping force results in shortened relaxation times and therefore lowers computational costs for simulations approaching mechanical equilibrium. The damping force on $\mathbf{p}(\mathbf{x}, t) \in D_i(t)$ due to $\mathbf{p}(\mathbf{y}, t) \in D_j(t)$ is given by

$$(4.5) \quad \mathbf{F}_d(\mathbf{y}, \mathbf{x}, t) = \begin{cases} -\beta_d \left(\frac{\mathbf{v}(\mathbf{y}, \mathbf{x}, t)}{|\mathbf{v}(\mathbf{y}, \mathbf{x}, t)|} \cdot \mathbf{e}(\mathbf{y}, \mathbf{x}, t) \right) \mathbf{e}(\mathbf{y}, \mathbf{x}, t) V_{\mathbf{x}} V_{\mathbf{y}} & \text{if } |\mathbf{p}(\mathbf{y}, t) - \mathbf{p}(\mathbf{x}, t)| < R_c \\ 0 & \text{otherwise} \end{cases}$$

where β_d is the damping coefficient given by $\beta_d = 2r_d \sqrt{\frac{K_n \rho}{V_{\mathbf{y}}}}$ and $r_d \in [0, 1]$ is the damping ratio. The combined damping forces acting on the point $\mathbf{p}(\mathbf{x}, t) \in D_i(t)$ due to all other particles is therefore given by

$$(4.6) \quad \sum_{j \neq i} \int_{\{\mathbf{y} \in D_j: |\mathbf{p}(\mathbf{y}, t) - \mathbf{p}(\mathbf{x}, t)| < R_c\}} \mathbf{f}_d(\mathbf{y}, \mathbf{x}, t) dV_{\mathbf{y}}, \quad \text{where } \mathbf{f}_d = \frac{\mathbf{F}_d}{V_{\mathbf{x}}}.$$

The expression for the damping coefficient β_d is derived from the Kelvin-Voigt model for a damped spring [18]. Combining [Equation \(4.1\)](#) and [Equation \(4.5\)](#), the magnitude of the pairwise damped repulsion force on $\mathbf{p}(\mathbf{x}, t)$ due to $\mathbf{p}(\mathbf{y}, t)$ in the direction $\mathbf{e}(\mathbf{y}, \mathbf{x}, t)$ is given by $-K_n V_{\mathbf{y}} V_{\mathbf{x}} (R_c - |\mathbf{p}(\mathbf{y}, t) - \mathbf{p}(\mathbf{x}, t)|) - \beta_d V_{\mathbf{y}} V_{\mathbf{x}} \mathbf{v}_n(\mathbf{y}, \mathbf{x}, t)$, where $\mathbf{v}_n(\mathbf{y}, \mathbf{x}, t) = \frac{\mathbf{v}(\mathbf{y}, \mathbf{x}, t)}{|\mathbf{v}(\mathbf{y}, \mathbf{x}, t)|} \cdot \mathbf{e}(\mathbf{y}, \mathbf{x}, t)$ and is equivalent to that of a viscoelastic spring connecting $\mathbf{p}(\mathbf{x}, t)$ and $\mathbf{p}(\mathbf{y}, t)$ with reference length R_c , spring constant $k = K_n V_{\mathbf{y}} V_{\mathbf{x}}$, and damping coefficient $c = \beta_d V_{\mathbf{x}} V_{\mathbf{y}}$. In terms of the damping ratio r_d , the damping coefficient is written as $c = 2r_d \sqrt{K_n V_{\mathbf{x}}^2 V_{\mathbf{y}} \rho}$, which implies $\beta_d = 2r_d \sqrt{\frac{K_n \rho}{V_{\mathbf{y}}}}$. When damping is absent, (i.e. $r_d = 0$), we have pairwise conservation of energy

$$\frac{d}{dt} \left(\frac{1}{2} \rho V_{\mathbf{x}} |\mathbf{v}_n(\mathbf{y}, \mathbf{x}, t)|^2 + \frac{1}{2} k (R_c - |\mathbf{p}(\mathbf{x}, t) - \mathbf{p}(\mathbf{y}, t)|)^2 \right) = 0.$$

In the presence of damping, the energy dissipation rate is given by

$$\frac{d}{dt} \left(\frac{1}{2} \rho V_{\mathbf{x}} |\mathbf{v}_n(\mathbf{y}, \mathbf{x}, t)|^2 + \frac{1}{2} k (R_c - |\mathbf{p}(\mathbf{x}, t) - \mathbf{p}(\mathbf{y}, t)|)^2 \right) = -c |\mathbf{v}_n(\mathbf{y}, \mathbf{x}, t)|^2.$$

The damping force acts in the opposite direction of $\mathbf{e}(\mathbf{y}, \mathbf{x}, t)$ and the magnitude of the damping force depends on the magnitude of normal projection of relative velocity. A nonlinear damping model such as [19] can be considered but we do not consider that here. We remark that introducing such damping forces between the material points within the same particle leads to a viscoelastic material model [38].

It is remarked that our contact model is an improvement of the one used in [20], where a particle damping is implemented on the centroid of the particle and is dependent on the mean velocity of the nodes in a particle. The damping model presented here enables us to specify the physical law of damping at the nodal (local) level that manifests in particle level (global) damping. The law also applies to nodes that have undergone damage and are isolated from its parent particle.

4.4. Self-contact. The presence of a peridynamic bond between two material points from the same parent particle provides the necessary repulsive force to ensure that the points do not overlap numerically. However, such repulsive forces are absent when the peridynamic bond between the points is broken. Therefore, we specify a self-contact law between nodes of the same parent particle which are not connected by a peridynamic bond but are close to each other due to large deformations. This is especially important for preventing the numerical inter-penetration of different parts of nonconvex particle shapes, and for modeling the contact between various broken segments of a parent particle where a peridynamic force is absent.

Our self-contact law depends on the distance between nodes in the reference (undeformed) configuration. If there is no peridynamic bond between two nodes \mathbf{x} and \mathbf{y} from the same parent particle D_i at time t and the current distance between them is within R_c (i.e. if $|\boldsymbol{\xi} + \boldsymbol{\eta}| < R_c$), the normal repulsive force on \mathbf{x} due to \mathbf{y} is given by

$$\mathbf{f}_r^{\text{self}}(\mathbf{x}, \mathbf{y}, t) = \begin{cases} c_w \frac{|\boldsymbol{\xi} + \boldsymbol{\eta}| - |\boldsymbol{\xi}|}{|\boldsymbol{\xi}|} \frac{\boldsymbol{\xi} + \boldsymbol{\eta}}{|\boldsymbol{\xi} + \boldsymbol{\eta}|} \chi_{\{|\boldsymbol{\xi} + \boldsymbol{\eta}| < |\boldsymbol{\xi}|\}}, & \text{if } |\boldsymbol{\xi}| < R_c \\ c_w \frac{|\boldsymbol{\xi} + \boldsymbol{\eta}| - R_c}{R_c} \frac{\boldsymbol{\xi} + \boldsymbol{\eta}}{|\boldsymbol{\xi} + \boldsymbol{\eta}|} \chi_{\{|\boldsymbol{\xi} + \boldsymbol{\eta}| < R_c\}}, & \text{if } R_c < |\boldsymbol{\xi}|, \end{cases}$$

where χ_S is the characteristic function of the set S .

Note that in the small reference length scale $|\boldsymbol{\xi}| < R_c < \epsilon$, the repulsive contact force is modeled using a repulsive-only peridynamic bond force. This ensures that two nodes with reference distance $|\boldsymbol{\xi}| < R_c$ do not experience any repulsive force from each other unless they come closer than their reference distance $|\boldsymbol{\xi}|$. If $|\boldsymbol{\xi}| > R_c$, the contact force between nodes from the same parent particle is same as the contact force between nodes from different parent particles if $\frac{c_w}{R_c} = K_n$.

4.5. Contact with wall. In earlier works [20, 2], the wall of the container containing all the particles is treated as a peridynamic domain. For our purposes, the wall is considered to be rigid (i.e., not deformable) and of thickness at least $\frac{R_c}{2}$. The inner boundary of the container wall is assumed to be rectangular, consisting of straight lines $L = \{l_i\}_{i=1}^4$. The point $\mathbf{p}(\mathbf{x}, t)$ inside the particle $D_k(t)$ experiences contact force due the wall if there exists $l \in L$ such that the perpendicular distance from $\mathbf{p}(\mathbf{x}, t)$ to l is smaller than the contact radius R_c . In this case, we denote the set of all wall points exerting contact force on $\mathbf{p}(\mathbf{x}, t)$ by the set $S_l(\mathbf{x}, t)$, which is a

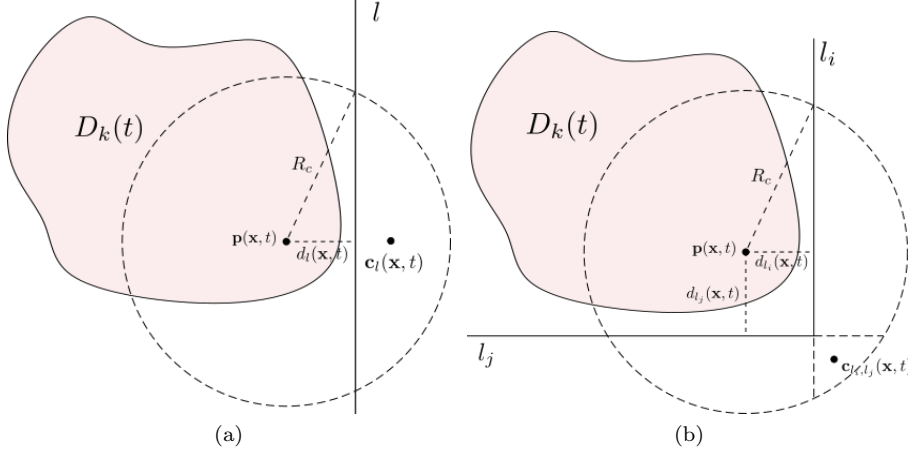


Fig. 2: Computation of wall contact volume and the centroid of wall volume responsible for exerting contact forces for contact with (a) single and (b) double wall boundaries. The contact radius is exaggerated to show the quantities of interest.

circular segment of the disk $B_{R_c}(\mathbf{p}(\mathbf{x}, t))$. In this case, the repulsive force due to the wall on $\mathbf{p}(\mathbf{x}, t)$ is given by

$$(4.7) \quad \mathbf{F}_r^l(\mathbf{x}, t) = \begin{cases} -K_n(R_c - |\mathbf{c}_l(\mathbf{x}, t) - \mathbf{p}(\mathbf{x}, t)|)V_{\mathbf{x}} |S_l(\mathbf{x}, t)| \mathbf{e}^l(\mathbf{x}, t) & \text{if } d_l(\mathbf{x}, t) < R_c \\ 0 & \text{otherwise,} \end{cases}$$

where $|S_l(\mathbf{x}, t)|$ is the volume of $S_l(\mathbf{x}, t)$, $\mathbf{c}_l(\mathbf{x}, t)$ is the centroid of $S_l(\mathbf{x}, t)$, and $d_l(\mathbf{x}, t)$ is the distance from $\mathbf{p}(\mathbf{x}, t)$ to l (see Figure 2a). $\mathbf{e}^l(\mathbf{x}, t)$ is the unit vector in the direction $\mathbf{c}_l(\mathbf{x}, t)$ from $\mathbf{p}(\mathbf{x}, t)$ given by $\mathbf{e}^l(\mathbf{x}, t) = \frac{\mathbf{c}_l(\mathbf{x}, t) - \mathbf{p}(\mathbf{x}, t)}{|\mathbf{c}_l(\mathbf{x}, t) - \mathbf{p}(\mathbf{x}, t)|}$ and determines the direction of repulsive wall force on $\mathbf{p}(\mathbf{x}, t)$.

Near the corner of a rectangular container, the point $\mathbf{p}(\mathbf{x}, t)$ will experience contact forces from two inner wall boundary segments l_i and l_j if $d_{l_i, l_j}(\mathbf{x}, t) := \sqrt{d_{l_i}^2(\mathbf{x}, t) + d_{l_j}^2(\mathbf{x}, t)} < R_c$ (see Figure 2b). In this case, the repulsive force on $\mathbf{p}(\mathbf{x}, t)$ due to the wall is given by $\mathbf{F}_r^{l_i \cup l_j}(\mathbf{x}, t) = \mathbf{F}_r^{l_i}(\mathbf{x}, t) + \mathbf{F}_r^{l_j}(\mathbf{x}, t) - \mathbf{F}_r^{l_i, l_j}(\mathbf{x}, t)$, where

$$\mathbf{F}_r^{l_i, l_j}(\mathbf{x}, t) = -K_n(R_c - |\mathbf{c}_{l_i, l_j}(\mathbf{x}, t) - \mathbf{p}(\mathbf{x}, t)|)V_{\mathbf{x}} |S_{l_i, l_j}(\mathbf{x}, t)| \mathbf{e}_{l_i, l_j}(\mathbf{x}, t),$$

$S_{l_i, l_j} = S_{l_i} \cap S_{l_j}$, $\mathbf{c}_{l_i, l_j}(\mathbf{x}, t)$ is the centroid of S_{l_i, l_j} , and $\mathbf{e}_{l_i, l_j}(\mathbf{x}, t) = \frac{\mathbf{c}_{l_i, l_j}(\mathbf{x}, t) - \mathbf{p}(\mathbf{x}, t)}{|\mathbf{c}_{l_i, l_j}(\mathbf{x}, t) - \mathbf{p}(\mathbf{x}, t)|}$. Therefore, for a rectangular wall boundary with straight line segments $\{l_i\}_{i=1}^4$, the repulsive contact force due to the wall boundary is given by

$$(4.8) \quad \mathbf{F}_r^{\text{wall}}(\mathbf{x}, t) = \sum_{i=1}^4 \mathbf{F}_r^{l_i}(\mathbf{x}, t) - \sum_{i < j} \mathbf{F}_r^{l_i, l_j}(\mathbf{x}, t).$$

The total friction and damping forces $\mathbf{F}_f^{\text{wall}}(\mathbf{x}, t)$ and $\mathbf{F}_d^{\text{wall}}(\mathbf{x}, t)$ due to the wall boundary can be computed accordingly from Equation (4.3) and Equation (4.5), respectively, by replacing $\mathbf{e}(\mathbf{y}, \mathbf{x}, t)$ by $\mathbf{e}^l(\mathbf{x}, t)$, $V_{\mathbf{y}}$ by $|S_l(\mathbf{x}, t)|$, and $\mathbf{p}(\mathbf{y}, t)$ by $\mathbf{c}_l(\mathbf{x}, t)$.

Since the wall boundaries are not deformable, the wall volumes $|S_l|$ and $|S_{l_i, l_j}|$ participating in exerting contact forces due to single and double wall boundaries can be computed analytically. This reduces the computational cost of the simulations as one does not need to discretize the wall during simulations. For the convenience of the reader, we present the analytical expressions here.

For a single-wall contact, the area of the circular segment S_l is given by

$$|S_l(\mathbf{x}, t)| = \frac{1}{2} \pi R_c^2 - R_c^2 \arcsin\left(\frac{d_l(\mathbf{x}, t)}{R_c}\right) - \sqrt{R_c^2 - d_l(\mathbf{x}, t)^2} d_l(\mathbf{x}, t)$$

and the distance from the point $\mathbf{p}(\mathbf{x}, t)$ to the centroid of $S_l(\mathbf{x}, t)$ is

$$|\mathbf{c}_l(\mathbf{x}, t) - \mathbf{p}(\mathbf{x}, t)| = \frac{2}{3} \frac{1}{|S_l(\mathbf{x}, t)|} (R_c^2 - d_l(\mathbf{x}, t)^2)^{\frac{3}{2}}.$$

Note that when $\mathbf{p}(\mathbf{x}, t)$ touches the wall boundary segment l we have $d_l(\mathbf{x}, t) = 0$, therefore the effective wall contact volume is $|S_l(\mathbf{x}, t)| = \frac{\pi R_c^2}{2}$, the area of the half-circle.

For the contact with two wall boundary segments l_i and l_j , the effective wall volume responsible for exerting contact force on $\mathbf{p}(\mathbf{x}, t)$ is $|S_{l_i}(\mathbf{x}, t) \cup S_{l_j}(\mathbf{x}, t)|$. We show how to compute the effective wall volume for this case. Using the inclusion-exclusion principle, we have $|S_{l_i}(\mathbf{x}, t) \cup S_{l_j}(\mathbf{x}, t)| = |S_{l_i}(\mathbf{x}, t)| + |S_{l_j}(\mathbf{x}, t)| - |S_{l_i}(\mathbf{x}, t) \cap S_{l_j}(\mathbf{x}, t)|$. Integrating in polar coordinates, we obtain

$$\begin{aligned} & |S_{l_i}(\mathbf{x}, t) \cap S_{l_j}(\mathbf{x}, t)| \\ &= -\frac{1}{2} R_c^2 \arcsin\left(\frac{d_{l_i}(\mathbf{x}, t)}{R_c}\right) + \frac{1}{2} R_c^2 \arcsin\left(\frac{\sqrt{R_c^2 - d_{l_j}(\mathbf{x}, t)^2}}{R_c}\right) \\ &\quad + d_{l_i}(\mathbf{x}, t) d_{l_j}(\mathbf{x}, t) - \frac{1}{2} \sqrt{R_c^2 - d_{l_i}(\mathbf{x}, t)^2} d_{l_i}(\mathbf{x}, t) - \frac{1}{2} \sqrt{R_c^2 - d_{l_j}(\mathbf{x}, t)^2} d_{l_j}(\mathbf{x}, t) \end{aligned}$$

Let the centroid of $S_{l_i}(\mathbf{x}, t) \cap S_{l_j}(\mathbf{x}, t)$ be denoted by $\mathbf{c}_{l_i, l_j}(\mathbf{x}, t)$. Then, we have

$$\mathbf{c}_{l_i, l_j}(\mathbf{x}, t) - \mathbf{p}(\mathbf{x}, t) = \frac{1}{|S_{l_i}(\mathbf{x}, t) \cap S_{l_j}(\mathbf{x}, t)|} \begin{bmatrix} I_x \\ I_y \end{bmatrix},$$

where the moments of inertia I_x and I_y are given by

$$\begin{aligned} I_x &= \frac{1}{6} d_{l_j}(\mathbf{x}, t)^3 - \frac{1}{2} (R_c^2 - d_{l_i}(\mathbf{x}, t)^2) d_{l_j}(\mathbf{x}, t) + \frac{1}{3} (R_c^2 - d_{l_i}(\mathbf{x}, t)^2)^{\frac{3}{2}} \\ I_y &= -\frac{1}{2} R_c^2 d_{l_i}(\mathbf{x}, t) + \frac{1}{6} d_{l_i}(\mathbf{x}, t)^3 + \frac{1}{2} d_{l_i}(\mathbf{x}, t) d_{l_j}(\mathbf{x}, t)^2 + \frac{1}{3} (R_c^2 - d_{l_j}(\mathbf{x}, t)^2)^{\frac{3}{2}}. \end{aligned}$$

Note that when $d_{l_i}(\mathbf{x}, t) = d_{l_j}(\mathbf{x}, t) = 0$, i.e., when the point $\mathbf{p}(\mathbf{x}, t)$ touches the wall corner, we have $|S_{l_i}(\mathbf{x}, t) \cap S_{l_j}(\mathbf{x}, t)| = \frac{\pi R_c^2}{4}$, the area of the quarter of the contact circle $B_{R_c}(\mathbf{p}(\mathbf{x}, t))$.

4.6. Combined model for the particle aggregate. The equation of motion for the particle aggregate can now be given explicitly. Combining all the forces, the

equation of motion of the points $\mathbf{p}(\mathbf{x}, t) \in D_i(t)$, $i = 1, \dots, N$ is given by

(4.9)

$$\begin{aligned} \rho \ddot{\mathbf{u}}(\mathbf{x}, t) &= \int_{H_\epsilon(\mathbf{x}) \cap D_i} \mathbf{f}(\mathbf{x}', \mathbf{x}, t) dV_{\mathbf{x}'} \\ &+ \int_{\{\mathbf{y} \in D_i : |\mathbf{p}(\mathbf{y}, t) - \mathbf{p}(\mathbf{x}, t)| < R_c\}} (\mathbf{f}_r^{\text{self}}(\mathbf{x}', \mathbf{x}, t) + \mathbf{f}_d^{\text{self}}(\mathbf{x}', \mathbf{x}, t) + \mathbf{f}_f^{\text{self}}(\mathbf{x}', \mathbf{x}, t)) dV_{\mathbf{x}'} + \mathbf{b}(\mathbf{x}, t) \\ &+ \sum_{j \neq i} \int_{\{\mathbf{y} \in D_j : |\mathbf{p}(\mathbf{y}, t) - \mathbf{p}(\mathbf{x}, t)| < R_c\}} (\mathbf{f}_r(\mathbf{y}, \mathbf{x}, t) + \mathbf{f}_d(\mathbf{y}, \mathbf{x}, t) + \mathbf{f}_f(\mathbf{y}, \mathbf{x}, t)) dV_{\mathbf{y}} \\ &+ \mathbf{f}_r^{\text{wall}}(\mathbf{x}, t) + \mathbf{f}_d^{\text{wall}}(\mathbf{x}, t) + \mathbf{f}_f^{\text{wall}}(\mathbf{x}, t), \text{ for } \mathbf{x} \in D_i(0), i = 1, \dots, N \end{aligned}$$

where $\mathbf{f}_r = \frac{\mathbf{F}_r}{V_{\mathbf{x}}}$, $\mathbf{f}_d = \frac{\mathbf{F}_d}{V_{\mathbf{x}}}$, and $\mathbf{f}_f = \frac{\mathbf{F}_f}{V_{\mathbf{x}}}$ are the repulsive, damping, and friction force density functions, respectively, and they all have the unit of force/volume². Here the wall forces are expressed as the body force densities $\mathbf{f}_r^{\text{wall}} = \frac{\mathbf{F}_r^{\text{wall}}}{V_{\mathbf{x}}}$, $\mathbf{f}_d^{\text{wall}} = \frac{\mathbf{F}_d^{\text{wall}}}{V_{\mathbf{x}}}$, and $\mathbf{f}_f^{\text{wall}} = \frac{\mathbf{F}_f^{\text{wall}}}{V_{\mathbf{x}}}$.

5. Peridynamic bonds in nonconvex domains. Nonconvex particle contacts were handled in DEM-based approaches recently using level sets [24] and using convex-gluing methods [13][32]. However, in the peridynamic treatment of nonconvex particles, a technical challenge arises where one needs to identify bonds that extend outside the domain. If the peridynamic domain D is nonconvex, there exists a material point $\mathbf{x} \in D$ such that for some $\mathbf{y} \in H_\epsilon(\mathbf{x})$ the straight line segment joining \mathbf{x} and \mathbf{y} extends beyond the domain D . In other words, there exists $t \in [0, 1]$ such that the convex combination $l_{\mathbf{x}, \mathbf{y}}(t) := \mathbf{x} + t(\mathbf{y} - \mathbf{x}) \notin D$. Since peridynamic force cannot extend beyond the domain boundary, the bond between \mathbf{x} and \mathbf{y} is considered broken in the reference configuration. For general peridynamic domain D , the definition of peridynamic horizon can thus be modified to $H_\epsilon(\mathbf{x}) = \{\mathbf{y} \in D : |\mathbf{y} - \mathbf{x}| \leq \epsilon\} \setminus C_{\mathbf{x}}$, where $C_{\mathbf{x}} = \{\mathbf{y} \in D : \exists t \in [0, 1] \text{ such that } l_{\mathbf{x}, \mathbf{y}}(t) \notin D\}$. Note that when D is convex, the set $C_{\mathbf{x}}$ is empty for all $\mathbf{x} \in D$.

Here, we outline a method to characterize the set $C = \cup_{\mathbf{x} \in D} C_{\mathbf{x}}$ by proving a method to determine whether a line segment with length less than ϵ between two points in the domain extends outside the domain. We refer to such line segments as *non-bonds*. As a first attempt, note that if a line segment extends outside the domain D , it intersects the domain boundary ∂D . However, the converse is not true, in particular, for line segments starting and ending on the boundary ∂D . Moreover, numerically detecting line segments that are part of the domain boundary ∂D by solving a linear system is sensitive to round-off error. Therefore, we take a different approach to characterize C . Our method involves checking the intersection with an extended domain boundary and the angle bisectors of nonconvex cusps of the boundary.

We work with a piecewise straight line approximation of the domain boundary ∂D . Let $\partial D \in \mathbb{R}^2$ be a closed polygon $\mathbf{p}^1 \mathbf{p}^2 \dots \mathbf{p}^n \mathbf{p}^1$ oriented in the counterclockwise direction. In other words, the boundary is given by the set $\partial D = \cup_{i \in \mathbb{Z}_n} \{l_{\mathbf{p}^i, \mathbf{p}^{i+1}}(t) : t \in [0, 1]\}$. Define the unit tangent to the line segment $\mathbf{p}^i \mathbf{p}^{i+1}$ as $\mathbf{v}_i = \frac{\mathbf{p}^{i+1} - \mathbf{p}^i}{|\mathbf{p}^{i+1} - \mathbf{p}^i|}$. We say the vertex \mathbf{p}^i is a *nonconvex cusp* if the angle between the vectors \mathbf{v}_{i-1} and \mathbf{v}_i is

obtuse, i.e., if $\mathbf{v}_{i-1} \times \mathbf{v}_i < 0$. At vertex \mathbf{p}^i we define the outward ‘normal’ \mathbf{n}_i given by (see Figure 3a)

$$\mathbf{n}_i = \begin{cases} \frac{-\mathbf{v}_{i-1} + \mathbf{v}_i}{|\mathbf{v}_{i-1} + \mathbf{v}_i|}, & \text{if } \mathbf{v}_{i-1} \times \mathbf{v}_i < 0 \\ \frac{\mathbf{v}_{i-1} + \mathbf{v}_i}{|\mathbf{v}_{i-1} + \mathbf{v}_i|}, & \text{if } \mathbf{v}_{i-1} \times \mathbf{v}_i > 0 \\ \begin{bmatrix} 0 & -1 \\ 1 & 0 \end{bmatrix} \mathbf{v}_i, & \text{if } \mathbf{v}_{i-1} \times \mathbf{v}_i = 0. \end{cases}$$

We remark here that the notion of unit normal at the point \mathbf{p}^i is not well-defined due to non-uniqueness. Therefore, we choose \mathbf{n}_i to be simply the unit vector in the direction of the bisector of the outer angle at \mathbf{p}^i . Extending ∂D in the outward normal direction, we obtain the extended boundary $\overline{\partial D}$ given by the polygon $\bar{\mathbf{p}}^1 \bar{\mathbf{p}}^2 \dots \bar{\mathbf{p}}^n \bar{\mathbf{p}}^1$, where $\bar{\mathbf{p}}^i$ is a δ -perturbation of the vertex \mathbf{p}^i in the outward normal direction \mathbf{n}_i given by $\bar{\mathbf{p}}^i = \mathbf{p}^i + \delta \mathbf{n}_i$ for some $\delta > 0$.

For a nonconvex cusp \mathbf{p}^i , we also define \mathbf{q}^i to be the point of intersection with the domain boundary ∂D , if it exists. i.e., $\mathbf{q}^i = \mathbf{p}^i + t_0 \mathbf{n}_i$ such that there exists $j \in \mathbb{Z}_n$ and $t_0, s \in [0, 1]$ such that $\mathbf{p}^i + t_0 \mathbf{n}_i = \mathbf{p}^j + s(\mathbf{p}^{j+1} - \mathbf{p}^j)$. If no such intersection exists, we define $t_0 = |\mathbf{p}^i| + \sup\{|\mathbf{x}| : \mathbf{x} \in D\}$. In that case, using the reverse triangle inequality we have $|\mathbf{q}^i| \geq \sup\{|\mathbf{x}| : \mathbf{x} \in D\}$, and therefore the line segment $\mathbf{p}^i \mathbf{q}^i$ does not extend beyond the minimal bounding circle of the domain D .

Now, if $\mathbf{y} \in C_{\mathbf{x}}$, the line segment $\mathbf{x}\mathbf{y}$ intersects either the outer angle bisectors $\mathbf{p}^i \mathbf{q}^i$ at a nonconvex cusp \mathbf{p}^i or the extended boundary segments $\bar{\mathbf{p}}^i \bar{\mathbf{p}}^{i+1}$ for some $i \in \mathbb{Z}_n$. This method leads to an effective detection of non-bonds to construct the peridynamic horizon, which is especially useful for a nonconvex domain D . Figure 3

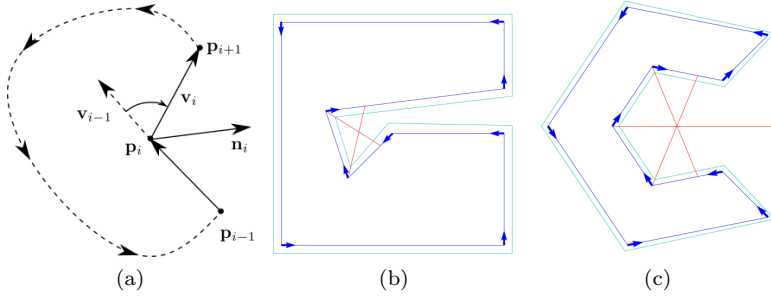


Fig. 3: (a) Unit outward normal \mathbf{n}_i at a domain boundary vertex (b),(c) Extended boundary and the angle bisector at nonconvex cusps for example particle boundary shapes.

demonstrates the construction of lines segments to intercept non-bonds in various nonconvex peridynamic domains. In the following sections, the finite element mesh generating software `Gmsh` [12] is used to obtain the nodes on and within the particle boundaries. The mesh size is defined as the minimum distance between any two nodes in all the particles in the simulation.

6. Simulations: two and three particle collisions. In this section, we first illustrate our method for handling intra-particle deformation and particle to particle interaction by solving the initial value problem Equation (4.9) for simple problems

with two and three particle interactions, $N = 2, 3$. [Subsection 6.1](#) provides a discussion of time integration and choice of time step used in all simulations. In [Subsection 6.2](#) we validate our dynamic fracture and contact model for nonconvex domains against the well-known Kalthoff-Winkler experiment [22]. In [Subsection 6.3](#) we illustrate the choice of peridynamic horizon and mesh size on elastic and inelastic deformation. In the last subsection [Subsection 6.4](#) we investigate crack initiation under compression for a pre-notched particle. We illustrate non-interpenetration of cracks and the calving of child particles by simulating a three particle initial value problem. Such behavior is essential to model comminution and crushing seen in aggregates.

We conclude the introduction listing particle dimensions and material properties used in all simulations used both in this section and the following section. The material properties of particles used in the simulations in [Section 6](#) and [Section 7](#) are listed as in [Table 2](#) as M_1 and M_2 , respectively.

Table 2: Common material properties used across simulations.

Material	Young's modulus (E)	Bulk modulus (k)	Density (ρ)
M_1	191×10^9 Pa	159.2×10^9 Pa	8000 kg/m ³
M_2	1.23×10^9 Pa	2×10^9 Pa	1200 kg/m ³

6.1. Time integration steps for N particles. To simulate the dynamics of the particle nodes, we use the Velocity-Verlet scheme [16]. In the reference configuration, we discretize all particles D_k $k = 1, 2, \dots, N$ in space. \mathbf{x} and \mathbf{y} denote generic nodes inside two distinct particles. A complete algorithm depicting the time integration steps with time step $\Delta t > 0$ involving neighborhood search and force computations is given in [Algorithm 6.1](#).

We take our time step Δt and mesh size h small enough to resolve all particle interactions for numerical stability as described in [5] and to simultaneously satisfy the nonlocal CFL condition that depends explicitly on the peridynamic horizon δ [21]. Applying this criterion we have chosen $\Delta t = 2.5$ ns for the two-particle tests in [Subsections 6.2](#) and [6.3](#), $\Delta t = 20$ ns for the three-particle test in [Subsection 6.4](#), and $\Delta t = 70$ ns for the bulk settling and compression tests in [Subsections 7.3](#) and [7.4](#). To fix ideas in this section we have chosen the friction and damping forces to be absent so $\mu = 0$ and $\beta_d = 0$. All friction and damping forces are active in the following [Section 7](#).

6.2. Collision with fracture and validation. Here, we validate our dynamic fracture and contact model for nonconvex domains against the well-known Kalthoff-Winkler experiment [22], where a cylindrical impactor strikes a plate with two existing notches, leading to a crack pattern that is experimentally reproducible. The schematic diagram is shown in [Figure 4a](#). The experiment has been simulated in [35, 41] with a mode II dynamic displacement condition which replaces the effect of the impactor. Here, we simulate the experiment as a two-particle collision problem, i.e., we solve [Equation \(4.9\)](#) for $N = 2$. Initially the impactor is traveling toward the plate at 32 meters per second. The notched particle is stationary with the corner left and right ligaments held fixed at the top. The impactor hits the central ligament. Using [Section 5](#) we remove the peridynamic bonds across the notches. Our simulation shown in [Figure 4b](#) is in good agreement with the experiment where the crack angle is observed to be roughly 68 degrees.

Algorithm 6.1 Time integration

-
- 1: Define $\mathbf{u}(\mathbf{x}), \dot{\mathbf{u}}(\mathbf{x}), \ddot{\mathbf{u}}(\mathbf{x}), \mathbf{b}(\mathbf{x})$ for $\mathbf{x} \in D_k$ at time $t = 0$ for $k = 1, 2, \dots, N$
 - 2: Compute intra-particle neighbors $S^{\text{ref}}(\mathbf{x}) = \{\mathbf{x}' \in D_k : |\mathbf{x} - \mathbf{x}'| < \epsilon\}$ for all $\mathbf{x} \in D_k, k = 1, 2, \dots, N$
 - 3: **while** $t < T$ **do**
 - 4: **for** $k = 1, 2, \dots, N$ and $\mathbf{x} \in D_k$ **do**
 - 5: $\mathbf{u}(\mathbf{x}) \leftarrow \mathbf{u}(\mathbf{x}) + \Delta t \dot{\mathbf{u}}(\mathbf{x}) + \frac{\Delta t^2}{2} \ddot{\mathbf{u}}(\mathbf{x})$ for $\mathbf{x} \in D_k$
 - 6: Compute current position $\mathbf{p}(\mathbf{x}) = \mathbf{x} + \mathbf{u}(\mathbf{x})$
 - 7: **end for**
 - 8: **for** $k = 1, 2, \dots, N$ and $\mathbf{x} \in D_k$ **do**
 - 9: Compute inter-particle neighbors $S_j^{\text{nbr}}(\mathbf{x}) = \{\mathbf{y} \in D_j : |\mathbf{p}(\mathbf{x}) - \mathbf{p}(\mathbf{y})| < R_c\}, j = 1, 2, \dots, N$
 - 10: Compute peridynamic force density $\mathbf{f}^{\text{peri}}(\mathbf{x}) = \sum_{\mathbf{x}' \in S^{\text{ref}}(\mathbf{x})} \mathbf{f}(\mathbf{x}', \mathbf{x}) V_{\mathbf{x}'}$
 - 11: Compute self-contact force density $\mathbf{f}^{\text{self}}(\mathbf{x}) = \sum_{\mathbf{x}' \in S_k^{\text{nbr}}} \left(\mathbf{f}_r^{\text{self}}(\mathbf{x}', \mathbf{x}) + \mathbf{f}_d^{\text{self}}(\mathbf{x}', \mathbf{x}) + \mathbf{f}_f^{\text{self}}(\mathbf{x}', \mathbf{x}) \right) V_{\mathbf{x}'}$
 - 12: Compute neighboring-particle force density $\mathbf{f}^{\text{nbr}}(\mathbf{x}) = \sum_{j \neq k} \sum_{\mathbf{y} \in S_j^{\text{nbr}}} (\mathbf{f}_r(\mathbf{y}, \mathbf{x}) + \mathbf{f}_d(\mathbf{y}, \mathbf{x}) + \mathbf{f}_f(\mathbf{y}, \mathbf{x})) V_{\mathbf{y}}$
 - 13: Compute wall-contact force density $\mathbf{f}^{\text{wall}}(\mathbf{x}) = \mathbf{f}_r^{\text{wall}}(\mathbf{y}, \mathbf{x}) + \mathbf{f}_d^{\text{wall}}(\mathbf{y}, \mathbf{x}) + \mathbf{f}_f^{\text{wall}}(\mathbf{y}, \mathbf{x})$
 - 14: Back up acceleration from previous time step: $\ddot{\mathbf{u}}^{\text{old}} := \ddot{\mathbf{u}}(\mathbf{x})$
 - 15: $\ddot{\mathbf{u}}(\mathbf{x}) \leftarrow \frac{1}{\rho} (\mathbf{f}^{\text{peri}}(\mathbf{x}) + \mathbf{f}^{\text{self}}(\mathbf{x}) + \mathbf{f}^{\text{nbr}}(\mathbf{x}) + \mathbf{f}^{\text{wall}}(\mathbf{x}) + \mathbf{b}(\mathbf{x}, t))$
 - 16: $\dot{\mathbf{u}}(\mathbf{x}) \leftarrow \dot{\mathbf{u}}(\mathbf{x}) + \frac{\Delta t}{2} (\ddot{\mathbf{u}}^{\text{old}} + \ddot{\mathbf{u}}(\mathbf{x}))$
 - 17: **end for**
 - 18: $t \leftarrow t + \Delta t$
 - 19: **end while**
-

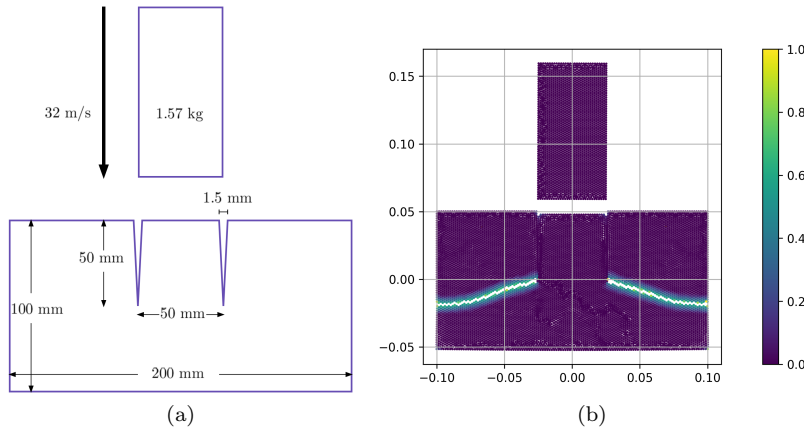


Fig. 4: (a) A schematic diagram of the Kalthoff-Winkler experiment (b) Simulation producing a crack angle of 68 degrees matching experimental results.

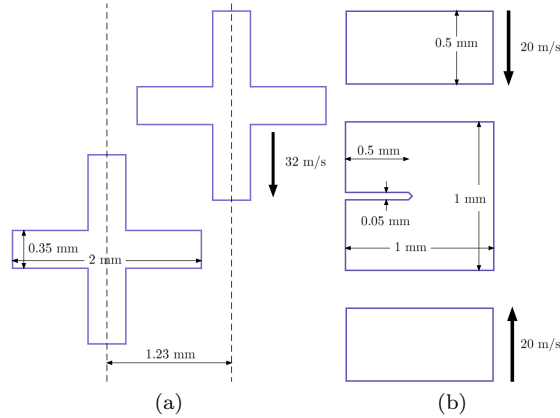


Fig. 5: Schematics of the two and three-particle collision tests.

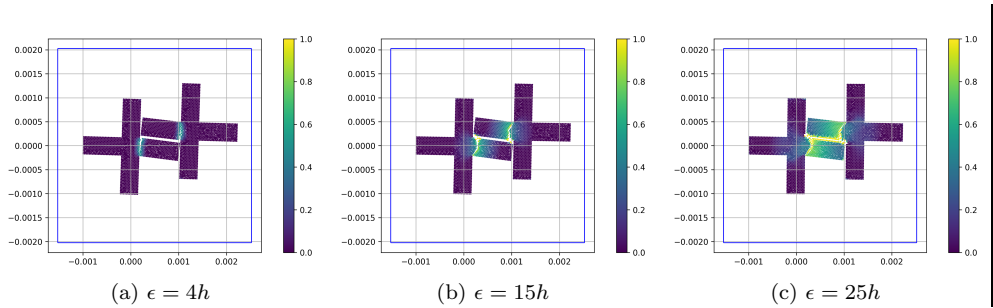


Fig. 6: Fracture patterns for varying peridynamic horizon size ϵ while the mesh size is fixed. Damage zone grows with horizon.

6.3. Study of peridynamic horizon size and mesh size on the damage of microscopic particles. We study the effect of the peridynamic horizon size ϵ and the mesh size h on **elastic and inelastic deformation** inside a particle. This effect is clearly exhibited for extreme particle deformation to the point of fracture and affects the location and extent of damage.

We consider a two-particle collision experiment in the millimeter length scale. In this experiment (see Figure 5a), a plus-shaped particle of half length $R = 1$ mm with arm width 0.35 mm traveling at the speed of 32 m/s collides with another cross at rest. The horizontal distance between the center of the particles is taken to be 1.23 mm. The fracture toughness of each particle is taken to be 424 Jm^{-2} . The mesh size is kept fixed at $h = \frac{R}{30}$, and we take the peridynamic horizon to be variable with $\epsilon = 4h, 15h$, and $25h$. The damage of the particle for each ϵ is shown in Figure 6.

For the next simulation, we fix the peridynamic horizon at $\epsilon = 0.133R$ mm, and decrease the mesh size. Figure 7 shows the damage of the particles for mesh size $h = \frac{R}{30}, \frac{R}{40}$, and $\frac{R}{50}$. We observe that for a fixed mesh size and increased peridynamic horizon size, the fracture patterns are less localized and spread over larger regions in the particle. However, particle-to-particle contact is dramatically influenced by

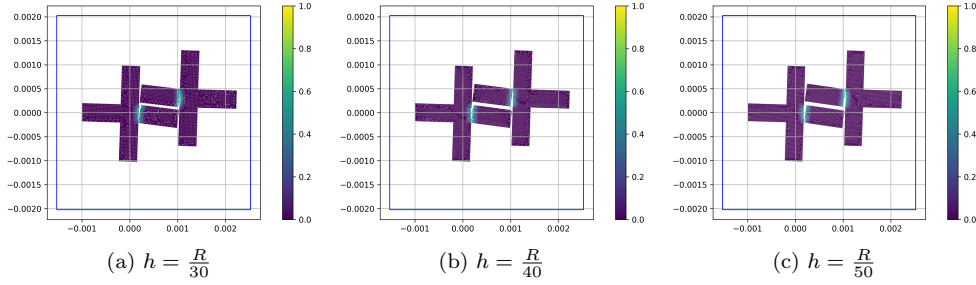


Fig. 7: Fracture patterns for varying mesh size h while the peridynamic horizon size is fixed. Damage zone remains localized in nearly the same location for this choice of mesh sizes.

the particle geometry, in particular, the presence of re-entrant corners influence the location of the fracture zone, as the contact forces are determined by a contact radius that is significantly smaller than the peridynamic horizon size.

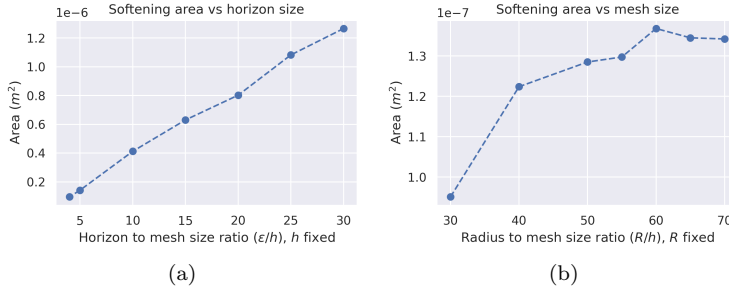


Fig. 8: Convergence of softening zone for (a) vanishing horizon ϵ and (b) vanishing mesh size h .

After 20 time steps (i.e. after 400 ns), the area of the softening zone in the first particle is computed for each simulation. The softening zone is defined by all points in the particle with nonzero damage. Consistent with theory [26], in the vanishing horizon limit $\epsilon \rightarrow 0$, the area of the softening zone converges to zero (see Figure 8a) when the mesh size remains fixed at $h = \frac{R}{30}$, leading to a fracture path of codimension 1. For the fixed horizon size ($\epsilon = 0.133R$) simulations (Figure 8b), the area of the softening zone converges to a fixed value as the mesh size h approaches zero.

6.4. Simulation: fracture toughness and damage propagation. Here, we study the effect of fracture toughness on crack patterns on particles with an existing pre-notch observed from a symmetric impact. In this experiment, (see Figure 5b) we consider a square-shaped particle (particle A) with length 1 mm with a pre-existing notch of length 0.5 mm that extends to the center of the particle. All peridynamic bonds that run across the pre-notch are removed in the reference configuration. Two rectangular particles (particles B and C) with dimension 1 mm \times 0.5 mm with velocities 20 m/s and -20 m/s, respectively, collide vertically with particle A simulta-

neously. Here damping and friction forces are turned off. We have taken 2 different values of fracture toughness for particle A. In [Figures 9a to 9d](#), the fracture toughness

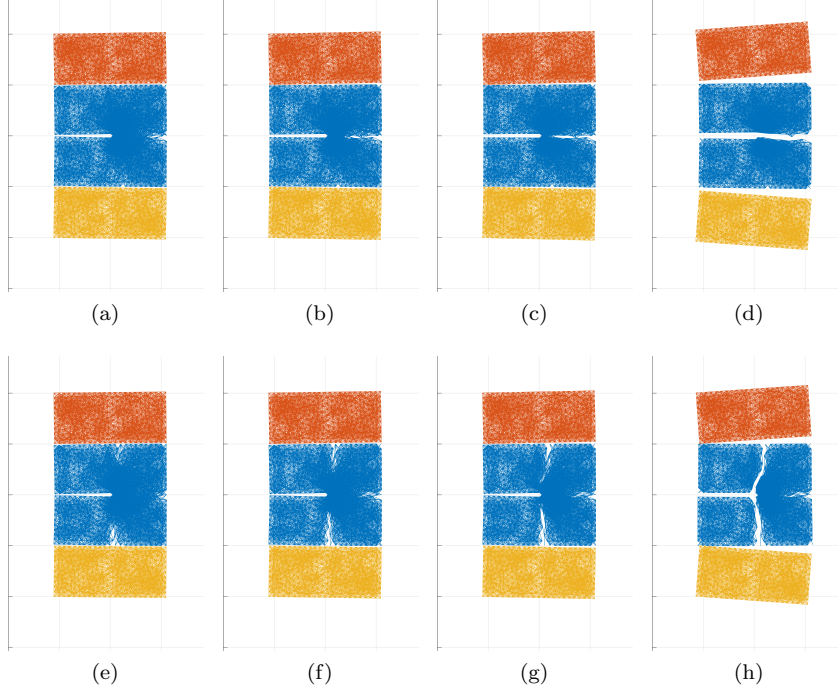


Fig. 9: Crack formation in domains with pre-notch for different fracture toughness. Figures in the top row correspond to $t = 29, 30, 31,$ and $50 \mu\text{s}$ after the simulation starts, and $t = 28, 29, 30,$ and $40 \mu\text{s}$ for the bottom row.

is taken to be $G_c = 135 \text{ J/m}^2$. We observe that a crack formed on the right edge of the particle propagates toward the tip of the pre-notch. When the crack tip reaches the tip of the pre-notch, particle A produces 2 disjoint child particles. In [Figures 9e to 9h](#), the fracture toughness is taken to be $G_c = 13.5 \text{ J/m}^2$, implying a softer particle. After the symmetric impact, 3 cracks are formed on the right, top, and bottom of the particle that propagate toward the crack tip. The cracks starting at the top and the bottom meet with the tip pre-notch simultaneously and before the crack from the right reaches the tip of the pre-notch. As a result, particle A is divided into 3 child particles, one of which (the one on the right) is partially cracked. Due to the stress concentration at the corners of the domains the corners are smoothed out upon impact. In [Figure 9](#) we have showed all the intact bonds present in the particles. The crack paths visualized here as an absence of peridynamic bonds emerge naturally from the progressive failure of bonds. Under the same experiment setup, the two different fracture patterns and the number of subsequent child particles generated after the collision are entirely determined by the fracture toughness G_c , which is a material property. It is important to observe that there is no interpenetration at the notch of particle A nor in the newly formed free surface of the cracks and child particles. This is due to the presence of self contact forces in the peridynamic model [Subsection 4.4](#) developed here.

7. Simulations: particle beds. In this section, we simulate the dynamic settling and compression of particle beds and illustrate the relative effects of different particle shapes and particle topology. We restrict ourselves to the two-dimensional case. The walls and floor of the particle bed container are modeled using straight lines and for consistency we will refer to surface area as “volume”. Wall-particle contact is computed in the way described in [Subsection 4.5](#). The domain containing the initial aggregate in a columnar configuration is denoted by Ω , see [Figure 12a](#). It has prescribed height and is bounded by a top horizontal edge, side walls and floor. The boundary is denoted by $\partial\Omega$. As mentioned earlier, it is essential to start the dynamics from an initial particle configuration that is agnostic to particle shape. To realize such a initial configuration we require the maximum cross-sectional diameter of every particle to be a fixed constant across all shapes. Additionally, the location of the center point of this diameter is prescribed so each particle experiences no interaction force from any other particle or the container walls. Lastly, the particles are randomly oriented. More generally, we will consider polydispersed aggregates consisting of particles of the same shape, which are initially free from contact forces and are randomly rotated about their centroids. Here “diameter” is short for the maximum diameter of a particle. The method accomplishes the following goals:

- A fast way to construct particle agnostic initial conditions for aggregates.
- A means to generate initial conditions to better understand macroscopic properties from microscopic dynamics of differently shaped particles.

The initial configuration is realized using the notion of security disks inside which the particle is placed. The size of the particle is chosen such that only its boundary has points in common with the boundary of the security disk. Each particle is randomly rotated about the center of its respective security disk. Next, we define the notion of jammed state for a disk (or sphere) packing of domains with disks of a finite number of different radii.

DEFINITION 7.1. *A domain packed with disjoint disks is in a jammed state if a displacement of any disk from its location causes it to overlap with another disk.*

With this in mind the location of the security disks are chosen such that by increasing all their radii by half the interaction radius R_c recovers a sphere packing that is in a jammed state. This provides the starting configuration for the dynamics. Other methods for doing this using more involved mesh-based packing of disks are possible resulting in higher packing densities, [25] but we do not apply them here. The specifics of the construction are given in the next section.

7.1. Generating an initial particle distribution. We present an algorithm for generating an initial distribution of particle sizes and locations of individual particles within an arbitrary region Ω independent of particle shape. The algorithm first constructs a jammed configuration of closed security disks and then decreases all their radii by half the interaction radius R_c . Last the particles are placed inside the security disks such their diameters match and are rotated randomly and independently.

1. Apply a prescribed discretization of Ω using finite-element mesh generating software. Here we use a triangular mesh.
2. Construct circles that are inscribed within triangular mesh elements contained in Ω . The location of the center of mass of a mesh triangle T with vertices $\mathbf{v}_1, \mathbf{v}_2, \mathbf{v}_3 \in \mathbb{R}^2$ is given by $\mathbf{c}_T = \frac{\mathbf{v}_1 l_1 + \mathbf{v}_2 l_2 + \mathbf{v}_3 l_3}{l_1 + l_2 + l_3}$ where $l_1 = |\mathbf{v}_2 - \mathbf{v}_3|$, $l_2 = |\mathbf{v}_1 - \mathbf{v}_3|$, and $l_3 = |\mathbf{v}_1 - \mathbf{v}_2|$. The radius is $r_T = \frac{2|T|}{l_1 + l_2 + l_3}$, where $|T|$ is the area of the triangle, see [Figure 10a](#).

3. Create nodal circles containing each node of the mesh in Ω such that they do not intersect with any of the inscribed circles of the neighboring triangles and do not overlap with the exterior of the domain Ω , see [Figure 10b](#).
4. Calculate centers and radius of nodal circles delivering a jammed configuration. Let $r(\mathbf{x}, \mathbf{c}) = |\mathbf{x} - \mathbf{c}|$ where \mathbf{c} is the center of any circle containing a node denoted by \mathbf{v} and \mathbf{x} is a point on the boundary of the circle. The constraints are 1) $r(\mathbf{x}, \mathbf{c}) \leq \rho_T(\mathbf{c})$ where T is any triangle with vertex \mathbf{v} and $\rho_T(\mathbf{c})$ is the distance between \mathbf{c} and the inscribed circle inside T ; 2) $r(\mathbf{x}, \mathbf{c}) \leq d(\mathbf{c}, e)$ where $d(\mathbf{c}, e)$ is the distance of \mathbf{c} to a boundary edge e . The radius $r_{\mathbf{v}}$ and center $\mathbf{c}_{\mathbf{v}}$ of each nodal circle for a jammed configuration is given by

$$r_{\mathbf{v}} = \max_{\mathbf{c}} \{ \max_{\mathbf{x}} \{ r(\mathbf{x}, \mathbf{c}) \wedge d(\mathbf{c}, e) \} \} \text{ and } \mathbf{c}_{\mathbf{v}} = \operatorname{argmax}_{\mathbf{x}} \{ \max_{\mathbf{c}} \{ r(\mathbf{x}, \mathbf{c}) \wedge d(\mathbf{c}, e) \} \}.$$

5. Reduce the radius of each security disk by $\frac{R_e}{2}$ so that contact forces are not activated.
6. Place particle of diameter equal to security disk inside and rotate randomly about center of security disk.

The optimization problem is solved numerically. In [Figure 10](#), we show the construction of a jammed packing from an arbitrary triangular mesh.

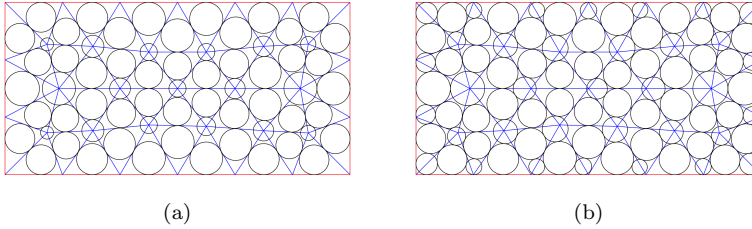


Fig. 10: Initial particle arrangement generation. Triangular mesh of the wall interior and the placement of inscribed circles for the triangles and initial placement nodal circles with packing ratio 0.69 ([Figure 10a](#)). Final jammed configuration of security disks obtained after maximizing the radii of the nodal circles including circles associated with the boundary nodes with packing ratio 0.80 ([Figure 10b](#)).

7.2. Construction of particle shapes. We consider particle aggregates consisting of particle shapes that are perturbed disks, square-shaped, plus-shaped, and annular or ring-shaped particles (see [Figure 11](#)). The particle shapes are chosen to study the effect of convexity, symmetry, and particle topology. The ring-shaped particles are rotationally symmetric, the square-shaped and plus-shaped particles have dihedral symmetry, and the perturbed disks are asymmetric. On the other hand, the plus-shaped particles and the perturbed disks are nonconvex, whereas the ring-shaped particles are nonconvex with a convex outer boundary. Therefore, by considering these shapes we provide a good variability of the key geometric and topological properties that influences the bulk behavior [[10](#), [9](#), [28](#)]. All shapes are inscribed in security disks using the method of [Subsection 7.1](#).

The non convex particle shapes including the perturbed disks and cross shapes are constructed by perturbing the boundary of a disk of radius R inward randomly. The vertices of the piece wise polynomial approximation to the particle boundary is given

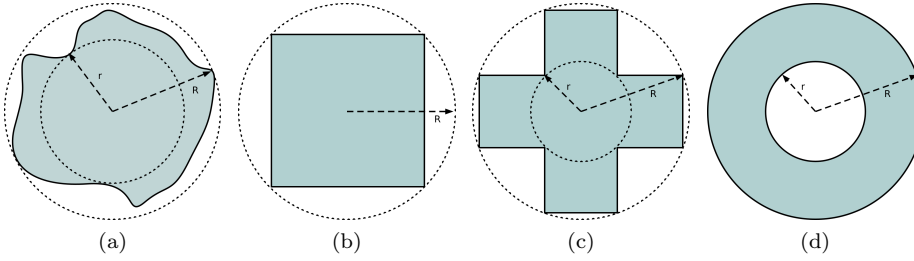


Fig. 11: Shapes of particles considered: perturbed disk, square, plus-shaped, and annular or ring-shaped particle. All shapes are inscribed in security disks using the method of [Subsection 7.1](#).

by the ordered set $\partial D = \{(r_i \cos \theta_i, r_i \sin \theta_i) : i = 1, \dots, N\}$, where $r_i = R(1 - X_i)$, where $\{X_i\}$ are independent and identically distributed uniform random variables on the interval $[0, 1 - \varphi]$. The roundness is measured by the ratio of the radii of the circles that can be inscribed within and can be circumscribed over the particle boundary. The average “roundness,” φ is taken to lie in the interval $\varphi \in [0, 1]$. For particles given by perturbed disks we apply piece wise linear approximations and have taken $N = 20$ and $\varphi = 0.6$. The square shapes are inscribed in the boundary of a security disk say of radius R hence the length of the side is $\sqrt{2}R$. For the plus-shaped particles we choose inner radius $r = cR$ with $c = 0.2$. For annular particles we take the inner radius to be $\tau \times$ outer radius with $\tau = 0.6$.

7.3. Particle bed settling under gravity. The dynamic settling of particle aggregates for different shapes and topology are simulated. Upon reaching equilibrium, the macroscopic properties given by height and total particle volume fraction are measured. For this case the volume fraction is the portion of the particle column occupied by particles. Here the volume of the particle column is given by the product of the height of the equilibrium configuration multiplied by the width of the container. The simulations illustrate the effect of the particle geometry and topology on the macroscopic quantity given by the particle volume fraction at equilibrium. Here, we consider 1490 particles of radii 0.4 mm - 1.1 mm (with mean 0.8 mm and standard deviation 0.09 mm) in a rectangular container of size 50 mm \times 100 mm and study the effect of particle shapes on the packing under a gravitational acceleration of 5000 m/s². The initial particle arrangement is generated using the technique discussed in [Subsection 7.1](#) so that each particle does not experience contact force from other particles or from the wall boundaries. After generating the positions of security disks containing particles so that they are jammed, we reduce the radii of the disks by $\frac{R_c}{2}$ so that no contact force is activated between particles. Here, the contact radius is taken to be $R_c = \frac{\epsilon}{5}$, and the mesh size is taken to be $h = \frac{\epsilon}{8}$, where $\epsilon = 0.5$ mm. Next, we apply a random rotation on the particles about their centroid. We activate the gravitational force and let the particles fall under their own weight. The particle bed is allowed to come to equilibrium until all oscillations of the aggregate decay to zero due to damping and friction force. Here we have taken $\mu = 0.8$ and $r_d = 0.8$. The jammed disk packing for the initial configuration is shown in [Figure 12a](#) and particle aggregates after coming to equilibrium are shown in [Figures 12b to 12e](#). The volume fraction ϕ is computed by taking the ratio of the combined particle volume

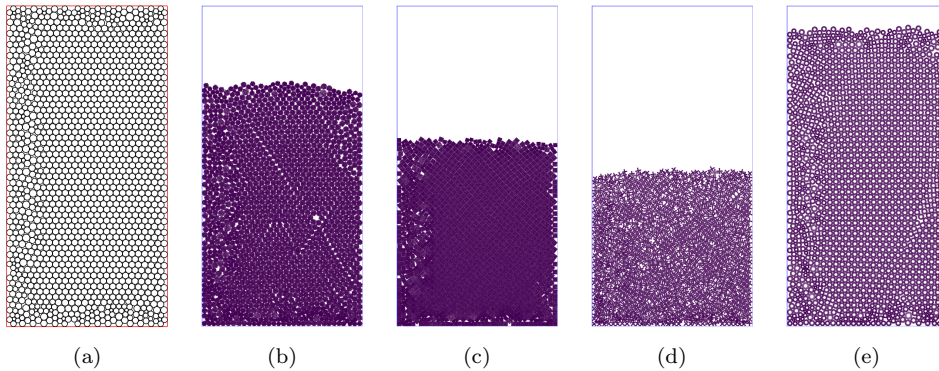


Fig. 12: The arrangement of security disks used to generate the initial particle arrangement (Figure 12a). Particles aggregates settle under gravity and in the presence of friction and damping force, and come to an equilibrium. The particle arrangement at equilibrium for aggregates consisting of perturbed disks, squares, plus-shaped and annular particles are shown in Figures 12b to 12e, respectively.

to the volume enclosed by the aggregate boundary. In Table 3, we show the change in the volume fraction between the initial and the fully settled configuration for different shapes. Here the particle shapes have been chosen to illustrate the effect

Table 3: Volume of individual particles and the bulk volume fraction at equilibrium.

Shape	Perturbed disk	Square	Plus	Annulus
Particle volume	$\pi R^2 \frac{(\varphi+1)^2}{4}$	$2R^2$	$c^2 R^2 (1 + 4\sqrt{\frac{2}{c^2} - 1})$	$\pi R^2 (1 - \tau^2)$
Initial ϕ	0.55	0.37	0.28	0.86
Equilibrium ϕ	0.75	0.64	0.59	0.92

of convexity, non convexity and topology on packing density. We find the volume fraction occupied by packed particles is lowest for plus particles followed by squares, perturbed disks, and annuli. The simple plus particle has the least packing fraction while the perturbed sphere has a packing fraction lying above the square. The ring has the largest volume fraction due to the extra excluded volume due to the interior hole. Among all shapes considered, the reduction of volume fraction of the loosely packed aggregate due to gravity is seen to be the maximum for the the plus-shaped particles, and the minimum for the ring-shaped particles.

7.4. Bulk compaction with damage. Here, we study the effect of damage on the bulk behavior. For each shape described in Subsection 7.2 we consider a particle aggregate with 496 particles of radii 0.3 mm - 1.1 mm (with mean 0.7 mm and standard deviation 0.09 mm) in a rectangular container with height $h = 20$ mm and width $l = 20$ mm. The initial position and radii of the security disks for aggregates of differently shaped particles are taken to be the same. In each case, the top wall of the container is lowered at the speed of $v = 1$ m/s. Here, we allow the particles to experience damage, which is incorporated according to Subsection 3.1. Gravity is

ignored here, therefore the volume fraction is determined entirely by the position of the top wall boundary. The contact radius R_c , the contact parameters K_n, μ , and r_d are taken to be the same as in [Subsection 7.3](#).

The volume fraction is given by the ratio of the total particle volume and the volume of the container. Therefore, the volume fraction in our simulation as a function of time is given by $\phi(t) = \frac{\sum_{i=1}^N V_i}{l(h-vt)}$, where V_i is the volume of the i^{th} particle and N is the total number of particles. The *bulk damage* is defined as the average particle damage over all particles, whereas the *particle damage* is defined as the mean damage over all points in the particle.

7.4.1. Effect of particle shape. The initial setup and two snapshots of the simulations are shown in [Figure 13](#), where the damage value of each node of each particle is plotted. As the top wall boundary is lowered, particle aggregates become

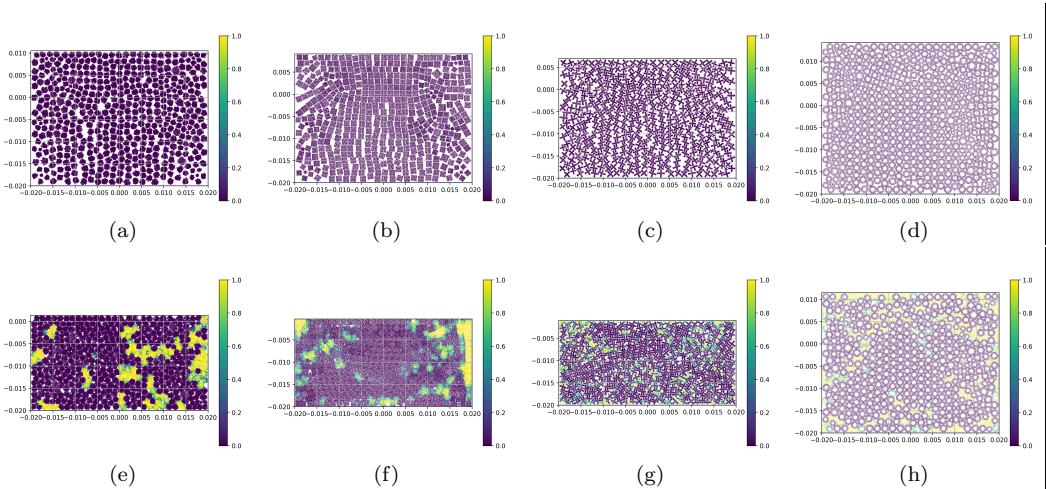


Fig. 13: Compression test on aggregates consisting of particles of various shapes where the top wall is lowered at speed 1 m/s. The bottom row shows the snapshot of the aggregate when the bulk damage reaches 0.2. The top row captures the formation of particle columns before any damage has set in. The damage value of each node of each particle is shown in color.

denser and eventually begin to break. In [Figures 13e to 13h](#) we show the snapshots of the aggregates when the bulk damage reaches 0.2. The simulation time corresponding to these snapshots are $0.018 \mu\text{s}$, $0.020 \mu\text{s}$, $0.021 \mu\text{s}$, and $0.009 \mu\text{s}$, respectively. An intermediate configuration of each aggregate is shown in [Figures 13a to 13d](#) where no damage has occurred but the particle bulk is compressed significantly. These snapshots are taken at $0.010 \mu\text{s}$, $0.011 \mu\text{s}$, $0.013 \mu\text{s}$, and $0.006 \mu\text{s}$ after the simulation starts. In this regime, particles form vertical columns that carry the primary mechanical load of the aggregate and eventually break down as some of the particles in these columns begin experiencing damage. The simulations are terminated when the bulk damage reaches 1. Since aggregates of various shapes get fully damaged (i.e. when the bulk damage reaches 1) at different volume fractions, the simulations stop at different times and volume fractions. The series of nodes that exert contact forces on each other via the particle columns form force chains [\[4\]](#). We observe that damage

is initiated along the force chains.

The bulk damage and the force exerted by the particle aggregate on the top wall are shown in Figure 14a and Figure 14b. We compare the mechanical response of

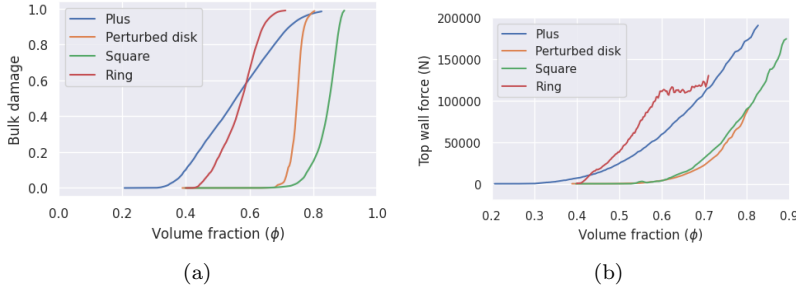


Fig. 14: Shape effect: bulk damage and force on the top wall exerted by aggregates of different shapes with respect to the volume fraction.

the bulk with respect to the volume fraction of the bulk. For the aggregate of plus particles the rate of damage with respect to the bulk volume fraction is the lowest among all shapes, but damage is initiated at the lowest volume fraction (at $\phi = 0.31$) compared to other shapes. The particle aggregate of squares experience initial damage at the highest volume fraction ($\phi = 0.71$) and the bulk damage rate with respect to the volume fraction is the highest. The aggregate of ring-shaped particles provide the highest bulk strength since it exerts the highest amount of force on the top wall. Particles with more excluded volume (i.e., the plus and ring-shaped particles) exert more wall force compared to the ones with less excluded volume (i.e., squares and perturbed disks) at the same volume fraction both in the damaged and undamaged regime. The aggregate with annular particles exhibits a unique non-increasing trend in the top wall force, which we investigate next.

7.4.2. Particle topology and effects due to damage and excluded volume. Here, we study the effect of particle topology, in particular, the presence of holes in particles. The holes can be regarded as excluded volumes in aggregates that are unable to participate in exerting contact forces provided the particles are not crushed. When the excluded volume in the particle aggregate is significant, after a certain amount of damage the wall contact force remains roughly constant even though the top wall keeps compressing the aggregate. This is observed for the aggregate of annular particles in Figure 14b between the volume fraction $\phi = 0.49$ and 0.7. During this “crushing” time, broken particle fragments are able to move into the region previously enclosed by the inner circles of the annuli. When crushing abates the wall reaction force starts increasing again.

We consider annular particles with inner circle radius r and outer circle radius R shown in Figure 11d. We define the *thinness* of the annular particle shown in Figure 11d as $\gamma = \frac{r}{R}$. Note that when $\gamma = 0$, the particle is a solid disk. While keeping the outer radius R fixed, we take annular particles with inner radius r to be $0.3R$, $0.4R$, \dots , $0.7R$, which correspond to $\gamma = 0.3, \dots, 0.7$, respectively. The wall contact force and the bulk damage for particles with various γ values are shown in Figure 15 with respect to time in Figures 15a and 15c and with respect to the bulk volume fraction in Figures 15b and 15d. The bulk damage rate with respect to

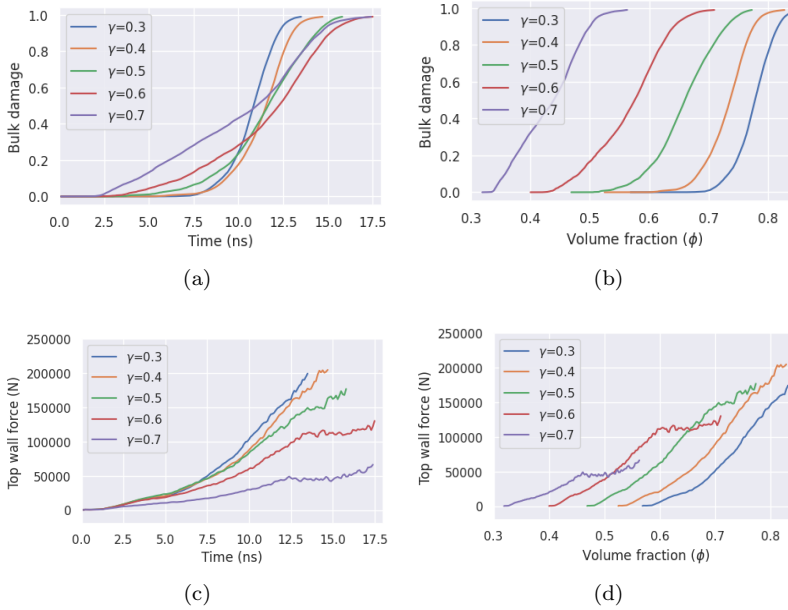


Fig. 15: Topology effect: damage and force on the top wall by aggregates consisting of annular particles with varying thickness γ .

both time and volume fraction is monotonically decreasing in thickness γ , i.e., particle aggregates with larger holes experience damage over a longer interval of time as well as volume fraction. Moreover, aggregates with thinner particles experience initial damage earlier and vice versa, which is observed in [Figure 15a](#).

Since the outer radius R is the same for all values of γ , the contact forces are activated at the same time across all aggregates. In general, for smaller values of γ the wall contact force is observed to be smaller. However, for particles with significant thickness (e.g. $\gamma > 0.5$) the excluded volume effect is more prominent where the wall contact force remains roughly constant even though the top wall keeps compressing the bulk (observed at $t = 13 \mu\text{s}$ for $\gamma = 0.6$ and at $t = 0.012 \mu\text{s}$ for $\gamma = 0.7$ in [Figure 15c](#)). During this time, broken particle fragments are able to occupy newly available excluded volume previously enclosed by the inner circles of the annuli without exerting additional force on the top wall as the bulk is compressed. As the aggregates are compressed further and the excluded volumes are filled up with particle fragments, the top wall force increases again (at $t = 0.017 \mu\text{s}$ for $\gamma = 0.6$ and $t = 0.018 \mu\text{s}$ for $\gamma = 0.7$ in [Figure 15c](#)). A similar trend is observed in [Figure 15d](#) where the top wall force is plotted with respect to the volume fraction.

8. Conclusion. In this work we provide a computational platform with stable implementation of inter-particle damping and friction to assess aggregate motion for particles of nonconvex shape. Peridynamics is coupled with DEM-like forces appropriately and the model is validated for collisions involving nonconvex domains against an experiment. We provide a method to automate the removal of peridynamic bonds to restrict the effect of nonlocal interactions within non-convex particles of arbitrary shapes. An algorithm to construct a jammed disk assembly is described to gener-

ate a shape-agnostic initial particle distribution for particle aggregate experiments. Damping is introduced as a nodal interaction as opposed to an approximation using the center of mass. Analytical expressions for wall-forces are derived to achieve higher accuracy not obtained by numerical approximation. The effect of particle shape on settling and compaction of aggregates of deformable particles is illustrated. Our method provides the opportunity to investigate the motion of the particle aggregate as a function of the physical properties of the individual particles including their shape, topology, elasticity, and strength.

REFERENCES

- [1] A. G. Athanassiadis, M. Z. Miskin, P. Kaplan, N. Rodenberg, S. H. Lee, J. Merritt, E. Brown, J. Amend, H. Lipson, and H. M. Jaeger. Particle shape effects on the stress response of granular packings. *Soft Matter*, 10(1):48–59, 2014.
- [2] M. Behzadinasab, T. J. Vogler, A. M. Peterson, R. Rahman, and J. T. Foster. Peridynamics Modeling of a Shock Wave Perturbation Decay Experiment in Granular Materials with Intra-granular Fracture. *J. dynamic behavior mater.*, 4(4):529–542, Dec. 2018.
- [3] F. Bobaru, M. Yang, L. F. Alves, S. A. Silling, E. Askari, and J. Xu. Convergence, adaptive refinement, and scaling in 1d peridynamics. *International Journal for Numerical Methods in Engineering*, 77(6):852–877, 2009.
- [4] J.-P. Bouchaud, P. Claudin, D. Levine, and M. Otto. Force chain splitting in granular materials: A mechanism for large-scale pseudo-elastic behaviour. *The European Physical Journal E*, 4(4):451–457, 2001.
- [5] S. J. Burns, P. T. Piironen, and K. J. Hanley. Critical time step for dem simulations of dynamic systems using a hertzian contact model. *International Journal for Numerical Methods in Engineering*, 119(5):432–451, 2019.
- [6] L. Campos, J. Oden, and N. Kikuchi. A numerical analysis of a class of contact problems with friction in elastostatics. *Computer Methods in Applied Mechanics and Engineering*, 34(1-3):821–845, 1982.
- [7] P. A. Cundall and O. D. L. Strack. A discrete numerical model for granular assemblies. *Géotechnique*, 29(1):47–65, Mar. 1979. Publisher: ICE Publishing.
- [8] P. S. Desai, A. Mehta, P. S. Dougherty, and C. F. Higgs. A rheometry based calibration of a first-order DEM model to generate virtual avatars of metal Additive Manufacturing (AM) powders. *Powder Technology*, 342:441–456, Jan. 2019.
- [9] K. Desmond and S. V. Franklin. Jammings of three-dimensional prolate granular materials. *Phys. Rev. E*, 73:031306, Mar 2006.
- [10] A. Donev, R. Connelly, F. H. Stillinger, and S. Torquato. Underconstrained jammed packings of nonspherical hard particles: Ellipses and ellipsoids. *Phys. Rev. E*, 75:051304, May 2007.
- [11] J. Finney. Random packings and the structure of simple liquids. I. The geometry of random close packing. *Proc. Roy. Soc. Lond. A*, 319:479–493, 1970.
- [12] C. Geuzaine and J.-F. Remacle. Gmsh: A 3-d finite element mesh generator with built-in pre- and post-processing facilities. *International journal for numerical methods in engineering*, 79(11):1309–1331, 2009.
- [13] N. Govender, D. N. Wilke, C.-Y. Wu, J. Khinast, P. Pizette, and W. Xu. Hopper flow of irregularly shaped particles (non-convex polyhedra): GPU-based DEM simulation and experimental validation. *Chemical Engineering Science*, 188:34–51, Oct. 2018.
- [14] Y. D. Ha and F. Bobaru. Studies of dynamic crack propagation and crack branching with peridynamics. *Int J Fract*, 162(1-2):229–244, Mar. 2010.
- [15] A. Hafez, Q. Liu, T. Finkbeiner, R. A. Alouhali, T. E. Moellendick, and J. C. Santamarina. The effect of particle shape on discharge and clogging. *Scientific Reports*, 11(1):3309, Feb. 2021. Number: 1 Publisher: Nature Publishing Group.
- [16] E. Hairer, C. Lubich, and G. Wanner. Geometric numerical integration illustrated by the Störmer–Verlet method. *Acta Numerica*, 12:399–450, May 2003. Publisher: Cambridge University Press.
- [17] J. M. Harmon, D. Arthur, and J. E. Andrade. Level set splitting in dem for modeling breakage mechanics. *Computer Methods in Applied Mechanics and Engineering*, 365:112961, 2020.
- [18] K. H. Hunt and F. R. E. Crossley. Coefficient of Restitution Interpreted as Damping in Vibroimpact. *Journal of Applied Mechanics*, 42(2):440–445, 06 1975.
- [19] R. Jankowski. Analytical expression between the impact damping ratio and the coefficient of restitution in the non-linear viscoelastic model of structural pound-

- ing. *Earthquake Engineering & Structural Dynamics*, 35(4):517–524, 2006. eprint: <https://onlinelibrary.wiley.com/doi/pdf/10.1002/eqe.537>.
- [20] P. K. Jha, P. S. Desai, D. Bhattacharya, and R. Lipton. Peridynamics-based discrete element method (PeriDEM) model of granular systems involving breakage of arbitrarily shaped particles. *Journal of the Mechanics and Physics of Solids*, 151:104376, June 2021.
- [21] P. K. Jha and R. Lipton. Numerical convergence of nonlinear nonlocal continuum models to local elastodynamics. *International Journal for Numerical Methods in Engineering*, 114(13):1389–1410, 2018.
- [22] J. F. Kalthoff. Modes of dynamic shear failure in solids. *International Journal of Fracture*, 101(1):1–31, 2000.
- [23] D. Kamensky, M. Behzadinasab, J. T. Foster, and Y. Bazilevs. Peridynamic modeling of frictional contact. *Journal of Peridynamics and Nonlocal Modeling*, 1(2):107–121, 2019.
- [24] R. Kawamoto, E. Andò, G. Viggiani, and J. E. Andrade. All you need is shape: predicting shear banding in sand with ls-dem. *Journal of the Mechanics and Physics of Solids*, 111:375–392, 2018.
- [25] C. Labra and E. Oñate. High-density sphere packing for discrete element method simulations. *Commun. Numer. Meth. Engng.*, 25(7):837–849, July 2009.
- [26] R. Lipton. Cohesive dynamics and brittle fracture. *Journal of Elasticity*, 124(2):143–191, 2016.
- [27] L. Liu, Z. Zhang, and A. Yu. Dynamic simulation of the centripetal packing of mono-sized spheres. *Physica A*, 268:433–453, 1999.
- [28] F. Ludewig and N. Vandewalle. Strong interlocking of nonconvex particles in random packings. *Phys. Rev. E*, 85:051307, May 2012.
- [29] S. Luding. Introduction to discrete element methods: Basic of contact force models and how to perform the micro-macro transition to continuum theory. *European Journal of Environmental and Civil Engineering*, 12(7-8):785–826, Aug. 2008.
- [30] J. Martins and J. Oden. A numerical analysis of a class of problems in elastodynamics with friction. *Computer Methods in Applied Mechanics and Engineering*, 40(3):327–360, 1983.
- [31] K. A. Murphy, K. A. Dahmen, and H. M. Jaeger. Transforming Mesoscale Granular Plasticity Through Particle Shape. *Phys. Rev. X*, 9(1):011014, Jan. 2019.
- [32] A. D. Rakotonirina, J.-Y. Delenne, F. Radjai, and A. Wachs. Grains3D, a flexible DEM approach for particles of arbitrary convex shape—Part III: extension to non-convex particles modelled as glued convex particles. *Comp. Part. Mech.*, 6(1):55–84, Jan. 2019.
- [33] A. Recuero, R. Serban, B. Peterson, H. Sugiyama, P. Jayakumar, and D. Negrut. A high-fidelity approach for vehicle mobility simulation: Nonlinear finite element tires operating on granular material. *Journal of Terramechanics*, 72:39–54, 2017.
- [34] K. K. Sahu. Gravity packing of same size spheres and investigation of wall ordering. *International Journal of Chemical Reactor Engineering*, 7:A70, 2009.
- [35] S. Silling. Dynamic fracture modeling with a meshfree peridynamic code. In K. Bathe, editor, *Computational Fluid and Solid Mechanics 2003*, pages 641–644. Elsevier Science Ltd, Oxford, 2003.
- [36] S. Silling and E. Askari. A meshfree method based on the peridynamic model of solid mechanics. *Computers & Structures*, 83(17-18):1526–1535, June 2005.
- [37] S. A. Silling. Reformulation of elasticity theory for discontinuities and long-range forces. *Journal of the Mechanics and Physics of Solids*, 48(1):175–209, Jan. 2000.
- [38] S. A. Silling. Attenuation of waves in a viscoelastic peridynamic medium. *Mathematics and Mechanics of Solids*, 24(11):3597–3613, Nov. 2019. Publisher: SAGE Publications Ltd STM.
- [39] S. A. Silling, M. Epton, O. Weckner, J. Xu, and E. Askari. Peridynamic States and Constitutive Modeling. *J Elasticity*, 88(2):151–184, Aug. 2007.
- [40] J. Trageser and P. Seleson. Bond-Based Peridynamics: a Tale of Two Poisson’s Ratios. *J Peridyn Nonlocal Model*, 2(3):278–288, Sept. 2020.
- [41] N. Trask, H. You, Y. Yu, and M. L. Parks. An asymptotically compatible meshfree quadrature rule for nonlocal problems with applications to peridynamics. *Computer Methods in Applied Mechanics and Engineering*, 343:151–165, 2019.
- [42] F. Zhu and J. Zhao. Modeling continuous grain crushing in granular media: A hybrid peridynamics and physics engine approach. *Computer Methods in Applied Mechanics and Engineering*, 348:334–355, May 2019.
- [43] F. Zhu and J. Zhao. A peridynamic investigation on crushing of sand particles. *Géotechnique*, 69(6):526–540, June 2019.